Mechanics of Materials 198 (2024) 105106

Contents lists available at ScienceDirect

Mechanics of Materials

journal homepage: www.elsevier.com/locate/mecmat

Research paper

Particle size effect on the thermoelastic behavior of composites—A comparative study between heterogeneous and homogenized beams

Jinming Zhang [a], Chunlin Wu [a,b,*], Huiming Yin [a]

[a] Department of Civil Engineering and Engineering Mechanics, Columbia University, 610 Seeley W. Mudd 500 West 120th Street, NY, 10027, United States
[b] Shanghai Institute of Applied Mathematics and Mechanics, School of Mechanics and Engineering Science, Shanghai University, Shanghai 200044, China

ARTICLE INFO

Keywords:
Size effect of inhomogeneity
Eshelby's equivalent inclusion method (EIM)
Thermoelastic behavior
Inclusion-based boundary element method (iBEM)
Representative volume element (RVE)

ABSTRACT

The particle size effect on the overall thermoelastic behavior of a composite containing many identical spherical particles reduces with the specimen-particle size ratio (SPR). When SPR is large enough, the effective stiffness converges, and the homogenized properties can represent the composite. This paper addresses two challenging questions: How large of an SPR is enough to reach the convergent results for different loading conditions, and whether is the critical SPR obtained from a uniform loading condition applicable to a nonuniform loading condition? When a uniform load is applied to a composite beam, the elastic moduli and thermal expansion coefficients can be calculated from the material's response. When the beam is subjected to pure or thermal bending, the deflection can be predicted by the heterogeneous or homogenized beams. The inclusion-based boundary element method (iBEM) is developed for high-fidelity simulation of many-particle systems. Given a volume fraction of particles, particle and beam size, and beam geometry, the local fields and the effective deformation are calculated for uniform and nonuniform loading conditions. The comparative study between a homogenized beam by the micromechanical approach and the numerical simulation of the heterogeneous particle system shows that a much larger SPR is required for thermal bending to reach a convergent result between the heterogeneous and homogenized beam. When the SPR is moderate, a cross-scale modeling method shall replace the micromechanical modeling to achieve accurate results.

1. Introduction

Composite materials combine two or more distinct constituent materials, such as fibers or particles in a matrix, and may achieve enhanced properties that a single-material phase cannot. Particulate composites have been widely used in machinery components like brake pads and engine components for improved durability and thermo-mechanical performance (Mura, 1987; Nemat-Nasser and Hori, 2013; Prasad et al., 1994; Campanella and Mitchell, 1968). The microstructure of composite materials, including particle size, volume fraction, and distribution, is crucial for determining their performance. Micromechanics of composites uses a representative volume element (RVE) to calculate the local field of a heterogeneous material system and predict the effective material behavior as a homogenized material (Hori and Nemat-Nasser, 1999; Yin and Zhao, 2016). Theoretically, the size of an RVE can be extended indefinitely to avoid the size effect. Numerically, the RVE should be constrained to a critical size that minimizes computational cost and secures a convergent solution.

The micromechanics-based approach typically involves two steps in applications: (1) use a uniform load, such as uniform far-field stress (Mura, 1987) in an RVE or uniform traction or displacement in a unit cell (Wu and Yin, 2021), to predict the effective material properties by the overall material response. Generally, the volume averages of the local fields are used to calculate the constitutive constants. (2) Homogenize the composite into a uniform material with the calculated constants for the actual design and analysis of the structure (Lee et al., 2019), so that the traditional structural design and analysis methods, such as the finite element method (FEM), can be used. Therefore, the design and applications of a complex material system can be simplified with micromechanical modeling. Two fundamental questions shall be addressed in this micromechanics-based approach: (1) What is the critical size of the RVE, which provides the minimal size of composite materials to assure the applicability of the micromechanical model? (2) Whether the critical RVE size under the uniform test loading condition applies to general loading conditions as well, which implies that the micromechanical model may still fail in some loading conditions if the required RVE size is larger?

* Corresponding author.
E-mail addresses: jinming.z@columbia.edu (J. Zhang), chunlinwu@shu.edu.cn (C. Wu), yin@civil.columbia.edu (H. Yin).

https://doi.org/10.1016/j.mechmat.2024.105106
Received 24 July 2024; Accepted 26 July 2024
Available online 5 August 2024

Several studies have addressed these questions. Hill (1963) first proposed that a composite sample, such as an RVE, should contain adequate microstructural details to sufficiently represent the composite. On the basis of Hill's concept, numerical studies have investigated size effects on RVE and mainly minimized its dimensions. Kanit et al. (2003) used a statistical approach to obtain RVE with tailorable and acceptable precision. In addition, a variational scheme (Terada et al., 2000) was applied to the homogenization process, examining the differences and convergences of parameters at macro and micro scales. Dirrenberger et al. (2014) concluded that larger RVEs generally exhibit slower convergence, causing difficulties in obtaining convergent results.

In actual applications, a composite can never be infinitely large, and the testing specimen and particle size difference can be quantified by the smallest dimension of the specimen versus the particle diameter, namely the specimen-particle size ratio (SPR). Recently, Wu and Yin (2021) conducted virtual experiments to investigate how microstructure affects overall homogenized properties, such as size variation and distribution of inhomogeneities. Specifically, Wu and Yin (2021) changed the number of stiffer inhomogeneities to understand the size effects, i.e., 8, 64, 125, 512, 1000 to 3375, while maintaining a constant volume fraction of 40%. The results of the virtual experiments indicate that the convergence of homogenized properties, such as elastic moduli, gradually decreases with smaller dimensions of inhomogeneities. In Wu's work (Wu and Yin, 2021), when the SPR is greater than 10, the difference in homogenized elastic moduli is below 1.4%.

Although some studies suggest that a greater SPR can improve the accuracy of homogenized properties, its applicability to general cases still needs to be investigated. Ostoja-Starzewski (1998) pointed out that improper selection and consideration of boundary conditions, especially scaling effects, can significantly alter local fields. Following this work, Alzebdeh et al. (1998) conducted several numerical studies on boundary conditions. Since homogenized properties are generally obtained from either virtual experiments or micromechanical theories, applications of the results to other loading conditions are open to question. Recently, Wu et al. (2023b) compared the deflection of a simply supported bilayered solar panel under downward pressure. The deflections are obtained through the substrate's actual microstructure or homogenized layer with uniform elastic constants obtained by micromechanical modeling. Surprisingly, the two solutions are fairly different, particularly in the maximum deflection, which motivates us to systematically investigate the applicability of micromechanical models at different SPR or RVE sizes.

Size effects in elasticity refer to the phenomenon in which the mechanical properties of a material or structure change as a function of its size, even when the material or structure is geometrically similar at different size scales. Three primary types of size effects are commonly observed: (1) For structural size effect, the size of a specimen affects the measured property, such as a decrease in strength or stiffness with increasing specimen size under an identical test condition (Wisnom, 1999; Bažant, 1999); (2) for surface-to-volume size effect, as the size of a material decreases, the ratio of its surface area to volume increases (Pan and Feng, 2008), which significantly influences properties such as thermal conductivity, electrical properties, and mechanical strength (Zhang et al., 2012); (3) microstructure size effect, which occurs when the characteristic size of microstructures, such as grains in a polycrystalline metal (Li et al., 2016) or fibers in a composite material (Xu et al., 1994), is so small that it creates different strain gradients and effective mechanical behavior.

This paper focuses on the microstructure size effect, quantified by the SPR for simplicity. The novelty of this study in comparison with the existing homogenization theory is the cross-scale modeling to determine the material behavior based on the actual microstructure and loading conditions, which does not satisfy the classic micromechanics assumptions but is too computationally expensive to be solved by existing numerical methods. It is discovered that a notably larger SPR is required to achieve convergent results between heterogeneous and homogenized beams for thermoelastic problems in comparison with the elastic or thermal problem. This shed light on limits of traditional homogenization theory on different boundary value problems. Note that in general continuum mechanics provides the same prediction of the effective material properties of particulate composites with the same distribution and volume fraction of particles but different size scales. Therefore, classic micromechanical models commonly avoid the microstructure size effect by assuming an infinitely large RVE. However, the particle size effect plays an important role in the experimental testing of composites due to particle interactions and boundary effects when SPR is moderate or relatively small (Barmouz et al., 2011).

Understanding how the size of particles or inclusions influences the overall behavior of the composite is vital for accurately characterizing and predicting its mechanical properties. Research has been conducted to estimate the influence of inclusion interaction on the macroscopic stiffness of the composite. This is achieved by considering multiple inclusion models, which serve as representative fragments of periodic inhomogeneities (Kushch, 1997, 2020). When particles are distributed in the form of a certain lattice, the composite inherently deviates from the isotropic assumption and the precise microstructure can be examined. By incorporating both the matrix and an adequate count of inhomogeneities, the cross-scale modeling considers any actual particle distribution.

This paper examines the effect of microstructure size in composite specimens under various loading conditions. For simplicity and repeatability, the periodic distribution of particles is studied. Section 2 introduces one composite sample containing inhomogeneities subjected to various thermal and mechanical loads in the remainder of the paper. Section 3 presents thermal, thermoelastic, and elastic fundamental solutions, and local fields disturbed by one inclusion with polynomial-form eigen-temperature gradient (ETG) and eigenstrain. Subsequently, the equivalent stress conditions of dual EIM (Wu et al., 2023a, 2024) are briefly introduced and implemented into the global matrix of the iBEM. Section 4 aims to validate the algorithm mentioned above by FEM by comparing local thermoelastic fields. Section 5 conducts virtual experiments to investigate the size effect where inhomogeneities exhibit uniform distribution with varying radii under the same volume fraction. Section 6 demonstrates the issue of homogenized properties with different test loads, where solutions with the actual microstructure exhibit significant differences. Finally, some conclusive remarks highlight the contrast in behavior between pure and thermal bending in homogenized and heterogeneous beams.

2. Problem statement

This study investigates the effect of particle size on the overall material behavior by analyzing a cuboid domain D containing multiple spherical inclusions Ω^I embedded in an isotropic matrix. Fig. 1 illustrates a beam of dimensions ($b \times h \times l$) containing spherical particles with a radius of a ($a < b = h < l$) at a volume fraction of ϕ. As the particle radius a decreases, the number of particles increases. The SPR is defined as b/a. The beam is the union of the inhomogeneities Ω^I and the matrix $D - \bigcup_{N_I} \Omega^I$. Each domain exhibits independent material properties, and its stiffness is denoted by C^m_{ijkl}, where $m = 0$ means the matrix, and $m = 1, 2, \ldots, N_I$ refer to the mth type of inhomogeneities. In actual composites, the inhomogeneities may exhibit the same radius and stiffness for simplicity, so $m = 0, 1$. Consider the matrix as an example. Its stiffness tensor C^0 is defined as $C^0 = \lambda^0 \delta_{ij}\delta_{kl} + \mu^0(\delta_{ik}\delta_{jl} + \delta_{il}\delta_{jk})$, where λ^0 and μ^0 are the Lamé parameters of the matrix. Similarly, K^0 is the thermal conductivity of the matrix, and the thermal modulus γ^0 is given by $\gamma^0 = (3\lambda^0 + 2\mu^0)\alpha^0$, where α^0 is the coefficient of thermal expansion (CTE).

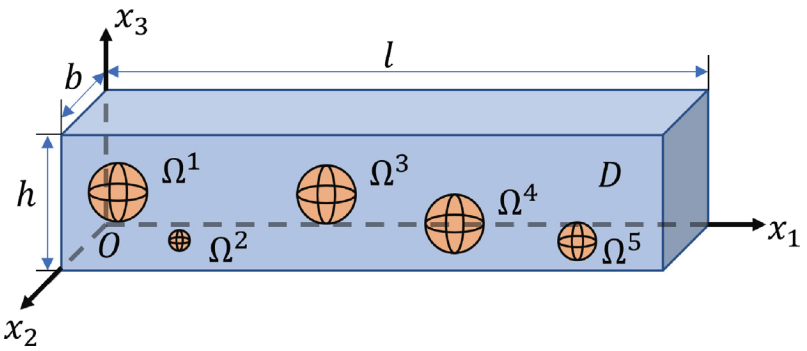

Fig. 1. Schematic illustration of a composite beam containing multiple spherical particles, where particles are arranged in a regular or random pattern.

Table 1
Material properties of aluminum and high-density polyethylene (HDPE).

Property	Aluminum	HDPE
Thermal conductivity (W/mK)	204	0.53
Coefficient of thermal expansion (CTE) (m/mK)	2.3×10^{-5}	1.2×10^{-4}
Young's modulus (GPa)	6.9	1.5
Shear modulus (GPa)	25.94	0.517

When the beam domain D is subjected to a specific load on the boundary, the load will be transferred to the particles and matrix. Assume that the inhomogeneities are perfectly bonded. The continuity of displacements, traction, temperature, and heat flux along the interfaces is written as:

$$\sigma_{ij}^{+}(\mathbf{x})n_j^{+} = \sigma_{ij}^{-}(\mathbf{x})n_j^{-}; \quad u_i^{+}(\mathbf{x}) = u_i^{-}(\mathbf{x}); \quad T^{+}(\mathbf{x}) = T^{-}(\mathbf{x}); \quad q_i^{+}(\mathbf{x}) = q_i^{-}(\mathbf{x}) \quad \text{on } \partial\Omega^I \tag{1}$$

where n_j is the normal vector of the inclusion interfaces $\partial\Omega^I$; the superscripts '−' and '+' indicate the inward and outward sides of the interfaces; u_i, σ_{ij}, T and q_i denote the displacement, stress, temperature, and heat flux, respectively.

For demonstration purposes, this paper follows our previous work using aluminum particles in a high-density polyethylene (HDPE) matrix for solar panel applications (Liu et al., 2015; Zhang et al., 2020; Yin et al., 2021). The material constants are provided in Table 1 (Haynes, 2014; Kováčik et al., 2018; Tavman, 1996). Following Mura's terminology (Mura, 1987), in this paper, inclusions denote material subdomains with the same material as the matrix but with a source field such as eigenstrain. In contrast, inhomogeneities encompass mismatches of material properties from the matrix.

Four loading conditions will be considered for the deformation of the beam:

(a) uniaxial loading with uniform stress at the two ends;

(b) pure bending with the moment applied at the two ends;

(c) uniform temperature change in the beam; and

(d) uniform transverse heat flow from the top to the bottom.

Loading (a) and (c) are uniform loading conditions. The average deformation can predict the elastic constants and thermal expansion coefficient, respectively, which can predict material behavior in loading (b) and (d) based on the micromechanics-based approach when the SPR is sufficiently large. However, the accuracy of this approach depends on the critical SPR value. The deflection of the beam will be investigated for both homogenized and heterogeneous material systems for conditions (b) and (d), which demonstrate the critical SPR value to make the micromechanics-based approach applicable.

Depending on the loading condition and the material's response, one can formulate the problem in three cases:

Case 1. The temperature field and heat flux caused by heat sources on the inhomogeneities or thermal loading on the boundary;

Case 2. The elastic fields caused by eigenstrain or force on the inhomogeneities or mechanical loading on the boundary;

Case 3. The thermoelastic field, such as thermal stress and strain, caused by heat sources on the inhomogeneities or thermal loading on the boundary.

3. Formulation of the problem

Eshelby's equivalent inclusion method (EIM) uses Green's function technique to solve the inclusion problem with an eigenstrain efficiently and thus set up the equivalence between an inclusion and an inhomogeneity by introducing an eigenstrain to simulate the material mismatch (Eshelby, 1957, 1959). Based on Eshelby's work on the elastic field in an ellipsoidal inclusion, the method is widely applied in composite material behavior and heterogeneous material property prediction.

3.1. Elastic and thermal fundamental solutions for a point source in the infinite domain

The EIM employs the Green's function technique based on the fundamental solutions. This method provides an elegant way to formulate complicated boundary value problems via superposition or integral of the response on the field caused by a distributed source field. Furthermore,

fundamental solutions yield valuable perspectives on the material's mechanical and thermal properties at the microscale level. In the field of isotropic thermoelasticity, Biot (1956) extended the Papkovitch–Neuber solution and obtained a solution comprising four potential functions. The completeness of Biot's general solution was subsequently proven by Verruijt (1969). Nowacki (1986) derived the full-space fundamental solution for a concentrated point heat source, and Barber (1992) provided a summary of the derivation for both two-dimensional (2D) and three-dimensional (3D) problems. Considering these fundamental solutions, the current approach initially reviews the formulation for thermal, elastic, and thermoelastic cases. In an infinite domain, fundamental solutions are obtained from a point heat source and a point force source, corresponding to the temperature field T and the displacement field $\mathbf{u}$, respectively. Specifically, the heat source influences T and $\mathbf{u}$, whereas the point force source exclusively affects $\mathbf{u}$. It is essential to highlight that the interaction between the heat source and $\mathbf{u}$ represents the thermoelastic coupling behavior, and it has commonly been solved with a thermal strain associated with the temperature field. Therefore, thermal and elastic analyses are completed. However, with the fundamental solution, the analysis can be significantly simplified.

Case 1: Thermal problem with a point heat source in the infinite domain

The temperature change can be written regarding the fundamental solution, known as the thermal Green's function. Let $\mathbf{x}' = (x_1', x_2', x_3')$ be the source point and $\mathbf{x} = (x_1, x_2, x_3)$ be the field point of interest. In the steady state with homogeneous thermal conductivity K^0, the governing equation in terms of the temperature field T is expressed as follows:

$$K^0 T_{,ii} + \dot{q}_V(\mathbf{x}) = 0 \tag{2}$$

where $\dot{q}_V$ represents the volumetric heat source. In the absence of $\dot{q}_V$, the heat conduction equation simplifies to the Laplace equation for a uniform material domain with constant K^0. For an arbitrarily distributed heat source $\dot{q}_V(\mathbf{x}')$, the temperature field is obtained by the integral of the Green's function as (Yin et al., 2022):

$$T(\mathbf{x}) = \int_\Omega G(\mathbf{x}, \mathbf{x}') \dot{q}_V(\mathbf{x}') d\mathbf{x}' \tag{3}$$

where $G(\mathbf{x}, \mathbf{x}')$ is the Green's function caused by a point heat source at $\mathbf{x}'$ as Eq. (4) and $\phi = |\mathbf{x} - \mathbf{x}'|^{-1}$ is the Newton potential.

$$G(\mathbf{x}, \mathbf{x}') = \frac{\phi}{4\pi K^0} \tag{4}$$

Case 2: Elastic problem with a point force in the infinite domain

The Navier equations describe the behavior of a uniform infinite domain subjected to a distributed force. The governing equation for this situation can be expressed as follows:

$$(\lambda^0 + \mu^0) u_{i,ij} + \mu^0 u_{j,ii} + b_j(\mathbf{x}) = 0 \tag{5}$$

where λ^0 and μ^0 denote the two Lamé constants of the elastic matrix material; u_i represents the ith displacement component; and $b_j(\mathbf{x})$ indicates the body force acting at $\mathbf{x}$ in jth direction. The displacement at any interior point can be expressed through the elastic Green's function $G_{ij}(\mathbf{x}, \mathbf{x}')$ as Eq. (6),

$$u_i(\mathbf{x}) = \int_\Omega G_{ij}(\mathbf{x}, \mathbf{x}') b_j(\mathbf{x}') d\mathbf{x}' \tag{6}$$

and

$$G_{ij}(\mathbf{x}, \mathbf{x}') = \frac{1}{4\pi\mu^0} \delta_{ij} \phi - \frac{1}{16\pi\mu^0(1-\nu^0)} \psi_{,ij} \tag{7}$$

where ν^0 denotes the Poisson's ratio of the elastic matrix material; δ_{ij} represents the Kronecker Delta, and; the function $\psi = |\mathbf{x} - \mathbf{x}'|$ is the biharmonic potential.

Case 3: Thermoelastic problem with a point heat source in the infinite domain

The temperature change caused by a point heat source in the infinite domain will produce thermal stress in the infinite domain. The constitutive relation is also known as the Duhamel–Neumann relation (Nowacki, 1986), written as:

$$\sigma_{ij} = 2\mu^0 \varepsilon_{ij} + (\lambda^0 \varepsilon_{kk} - \gamma^0 \Delta T) \delta_{ij} \tag{8}$$

and the strain tensor is defined as $\varepsilon_{ij} = \frac{1}{2}(u_{i,j} + u_{j,i})$. Using the following thermoelastic governing equation in coupling with Eq. (2):

$$(\lambda^0 + \mu^0) u_{i,ij} + \mu^0 u_{j,ii} - \gamma^0 T_{,j} = 0 \tag{9}$$

where $\gamma^0 = (3\lambda^0 + 2\mu^0)\alpha^0$ with α^0 indicating the CTE of the matrix, one can obtain:

$$(\lambda^0 + 2\mu^0) u_{i,ijj} + \frac{\gamma^0}{K^0} \dot{q}_V(\mathbf{x}) = 0 \tag{10}$$

Subsequently, the displacement field can be written as:

$$u_i(\mathbf{x}) = \int_\Omega G_i(\mathbf{x}, \mathbf{x}') \dot{q}_V(\mathbf{x}') d\mathbf{x}' \tag{11}$$

where $G_i(\mathbf{x}, \mathbf{x}')$ is the thermoelastic Green's function caused by a point force at $\mathbf{x}'$ as:

$$G_i(\mathbf{x}, \mathbf{x}') = \frac{\alpha^0}{8\pi K^0} \frac{1+\nu^0}{1-\nu^0} \psi_{,i} \tag{12}$$

where $\nu^0 = \frac{\lambda^0}{2(\mu^0+\lambda^0)}$ (Yin et al., 2022).

3.2. Thermomechanical fields caused by an inclusion with polynomial form sources

When a differentiable, continuous source field is applied in an inclusion, it can be approximately written in a polynomial form. For example, a polynomial form approximates the continuously distributed body force in the inclusion Ω^I as follows:

$$b_j(\mathbf{x}) = \begin{cases} B_j^{I0} + x_k B_{jk}^{I1} + x_k x_l B_{jkl}^{I2} + \cdots, & \mathbf{x} \in \Omega_I \\ 0, & \mathbf{x} \in D - \Omega_I \end{cases} \tag{13}$$

where the local coordinate is set with the origin at the center of the inclusion. The displacement field can be obtained by substituting Eq. (13) into Eq. (6) as follows:

$$\begin{aligned} u_i(\mathbf{x}) &= \int_{\Omega_I} G_{ij}(\mathbf{x},\mathbf{x}') b_j(\mathbf{x}') d\mathbf{x}' = \int_{\Omega_I} G_{ij}\left(B_j^{I0} + B_{jk}^{I1} x_k' + B_{jkl}^{I2} x_k' x_l' + \cdots\right) d\mathbf{x}' \\ &= \frac{1}{4\pi\mu^0}\delta_{ij}(\Phi B_j^{I0} + \Phi_k B_{jk}^{I1} + \Phi_{kl} B_{jkl}^{I2} + \cdots) - \frac{1}{16\pi\mu^0\left(1-\upsilon^0\right)}(\Psi_{,ij} B_j^{I0} + \Psi_{k,ij} B_{jk}^{I1} + \Psi_{kl,ij} B_{jkl}^{I2} + \cdots) \end{aligned} \tag{14}$$

where $\Phi, \Phi_k, \Phi_{kl}, \Psi_{,ij}, \Psi_{k,ij}$, and $\Psi_{kl,ij}$ are the integrals of $\phi, \phi x_k', \phi x_k' x_l', \psi_{,ij}, \psi_{,ij} x_k'$ and $\psi_{,ij} x_k' x_l'$ over the inclusion Ω^I, respectively (Yin et al., 2022). See Appendix for a spherical inclusion.

Given an ETG in the following polynomial form in the inclusion Ω^I:

$$T_i^*(\mathbf{x}) = T_i^{I0*} + x_k T_{ik}^{I1*} + x_k x_l T_{ikl}^{I2*} + \cdots \tag{15}$$

where $T^{I0*}i$, $T^{I1*}ik$, and T_{ikl}^{I2*} correspond to the uniform, linear, and quadratic terms of the ETG, respectively, we can then derive the resulting temperature field in terms of the ETG as follows

$$\begin{aligned} T(\mathbf{x}) &= -\int_{\Omega_I} G(\mathbf{x},\mathbf{x}') T_{i,i'}^*(\mathbf{x}') K(\mathbf{x}')\, d\mathbf{x}' \\ &= -\int_{\partial\Omega_I} G(\mathbf{x},\mathbf{x}') n_i' T_i^*(\mathbf{x}') K(\mathbf{x}')\, d\mathbf{x}' + \int_{\Omega_I} \frac{\partial G(\mathbf{x},\mathbf{x}')}{\partial x_i'} T_i^*(\mathbf{x}') K(\mathbf{x}')\, d\mathbf{x}' \\ &= -\int_{\Omega_I} \frac{\partial G(\mathbf{x},\mathbf{x}')}{\partial x_i} T_i^*(\mathbf{x}') K(\mathbf{x}')\, d\mathbf{x}' \\ &= -\int_{\Omega_I} G_{,i} K^0 (T_i^{I0*} + x_k' T_{ik}^{I1*} + x_k' x_l' T_{ikl}^{I2*} + \cdots)\, d\mathbf{x}' \\ &= f_i^{I0} T_i^{I0*} + f_{ik}^{I1} T_{ik}^{I1*} + f_{ikl}^{I2} T_{ikl}^{I2*} + \cdots \end{aligned} \tag{16}$$

in which $f_i^{I0} = -\int_\Omega G_{,i} K^0 d\mathbf{x}'$, $f_{ik}^{I1} = -\int_\Omega G_{,i} K^0 x_k' d\mathbf{x}'$, and $f_{ikl}^{I2} = -\int_\Omega G_{,i} K^0 x_k' x_l' d\mathbf{x}'$ are defined corresponding to the thermal Green's functions in Eq. (4). For a spherical inclusion, they are explicitly provided in Appendix.

Following the same fashion, given an eigenstrain as a source field in polynomial form in the inclusion Ω^I:

$$\varepsilon_{ij}^*(\mathbf{x}) = \varepsilon_{ij}^{I0*} + x_p \varepsilon_{ijp}^{I1*} + x_p x_q \varepsilon_{ijpq}^{I2*} + \cdots \tag{17}$$

we can derive the resulting displacement field as the integral of the eigenstrain:

$$\begin{aligned} u_i(\mathbf{x}) &= -\int_{\Omega_I} G_{ij}(\mathbf{x},\mathbf{x}') \varepsilon_{kl,m'}^*(\mathbf{x}') C_{jmkl}(\mathbf{x}')\, d\mathbf{x}' \\ &= -\int_{\Omega_I} \frac{\partial G_{ij}(\mathbf{x},\mathbf{x})}{\partial x_m'} \varepsilon_{kl}^*(\mathbf{x}') C_{jmkl}(\mathbf{x}')\, d\mathbf{x}' \\ &= -\int_{\Omega_I} G_{ij,m} C_{jmkl}^0 \varepsilon_{kl}^*(\mathbf{x}') (\varepsilon_{kl}^{I0*} + x_p' \varepsilon_{klp}^{I1*} + x_p' x_q' \varepsilon_{klpq}^{I2*} + \cdots)\, d\mathbf{x}' \\ &= g_{ikl}^{I0} \varepsilon_{kl}^{I0*} + g_{iklp}^{I1} \varepsilon_{klp}^{I1*} + g_{iklpq}^{I2} \varepsilon_{klpq}^{I2*} + \cdots \end{aligned} \tag{18}$$

where $g_{ikl}^{I0} = -\int_\Omega G_{ij,m} C_{jmkl}^0 d\mathbf{x}'$, $g_{iklp}^{I1} = -\int_\Omega G_{ij,m} C_{jmkl}^0 x_p' d\mathbf{x}'$, and $g_{iklpq}^{I2} = -\int_\Omega G_{ij,m} C_{jmkl}^0 x_p' x_q' d\mathbf{x}'$. See Appendix for a spherical inclusion.

Similarly, the displacement field caused by ETG in Eq. (15) can be written as:

$$\begin{aligned} u_i(\mathbf{x}) &= -\int_{\Omega_I} G_i(\mathbf{x},\mathbf{x}') T_{k,k'}^*(\mathbf{x}') K(\mathbf{x}')\, d\mathbf{x}' = -\int_{\Omega_I} \frac{\partial G_i(\mathbf{x},\mathbf{x}')}{\partial x_k} T_k^*(\mathbf{x}') K(\mathbf{x}')\, d\mathbf{x}' \\ &= -\int_{\Omega_I} G_{i,k} K^0 (T_k^{I0*} + x_p' T_{kp}^{I1*} + x_p' x_q' T_{kpq}^{I2*} + \cdots)\, d\mathbf{x}' \\ &= w_{ik}^{I0} T_k^{I0*} + w_{ikp}^{I1} T_{kp}^{I1*} + w_{ikpq}^{I2} T_{kpq}^{I2*} + \cdots \end{aligned} \tag{19}$$

where $w_{ik}^{I0} = -\int_\Omega G_{i,k} K^0 d\mathbf{x}'$, $w_{ikp}^{I1} = -\int_\Omega G_{i,k} K^0 x_p' d\mathbf{x}'$ and $w_{ikpq}^{I2} = -\int_\Omega G_{i,k} K^0 x_p' x_q' d\mathbf{x}'$ correspond to the thermoelastic Green's functions connecting ETG to displacement field, respectively. See Appendix for a spherical inclusion. Note that when the local coordinate is arbitrary, the polynomial form of $\mathbf{x}'$ should be referred to the center of the inclusion $\mathbf{x}^{Ic}$, so x_p' becomes $x_p' - x_p^{Ic}$.

3.3. Thermomechanical fields in a bounded material system with an inhomogeneity

Thanks to the technique of Green's function, BEM becomes a powerful tool for solving thermomechanical boundary value problems, including thermal and mechanical local fields. Using the thermal Green's function, the temperature field of the system can be determined, and temperature-induced mechanical effects are coupled through the boundary integral equations of thermoelastic Green's functions. This method is effective for materials as it greatly diminishes the need for extensive temperature volume integrals. For a heterogeneous material system, material mismatches

among inhomogeneities and matrix are simulated by the polynomial eigenstrain through continuously distributed fields. Due to the material mismatch between the inhomogeneity and the matrix, a disturbed field will be induced in the neighborhood of the inhomogeneity.

Eshelby (1957, 1959) proposed EIMs to solve the elastic inhomogeneity problem with the inclusion problem by introducing an eigenstrain on the inclusion to simulate the material mismatch. This approach can be extended to multiple inhomogeneities with the eigenstrain assumed in polynomial form. Wu and Yin (2021) proposed the iBEM algorithm for 2D and 3D linear elastic problems. Due to the versatility of Green's function, the authors (Yin et al., 2022) illustrate the iBEM algorithm with several multi-physical problems, such as steady-state heat transfer, Stokes flow. Recently, Yin's group (Wu et al., 2023a; Wang et al., 2022) derived modified bimaterial thermoelastic Green's functions, and proposed the dual equivalent inclusion method (DEIM) for handling thermoelastic inhomogeneities in a bi-material domain. When multiple particles are considered with boundary effects, the spatial variations of eigen-fields are not uniform anymore (Mura, 1987; Yin et al., 2022). However, they are still continuous and differentiable in the inhomogeneity domain with the material continuity in the particle. The polynomial form of eigen-fields can simulate the material mismatch with tailorable accuracy. Therefore, the Taylor series expansion of eigen-field in Eqs. (15) and (17), including uniform, linear and quadratic terms will be used in the calculation of local field. Moreover, Eshelby's equivalent conditions will be applied to determine the eigen-fields. Given that the equivalent inclusion involves mismatches in thermal and mechanical properties, the iBEM transforms temperature volume integrals into boundary integral equations and restricts domain integrals of ETG and eigenstrain to the inhomogeneity domains.

Case 1: iBEM for thermal problems

Combining the boundary integral equation of thermal Green's function and the disturbance from equivalent inclusions, the following thermal boundary integral equation can be formulated as (Yin et al., 2022):

$$\begin{aligned} T(\mathbf{x}) &= \int_{\partial D} G(\mathbf{x},\mathbf{x}')q(\mathbf{x}')d\mathbf{x}' - \int_{\partial D} H(\mathbf{x},\mathbf{x}')T(\mathbf{x}')d\mathbf{x}' - \int_{D} G_{,i}(\mathbf{x},\mathbf{x}')T_j^*(\mathbf{x}')K(\mathbf{x}')d\mathbf{x}' \\ &= \int_{\partial D} G(\mathbf{x},\mathbf{x}')q(\mathbf{x}')d\mathbf{x}' - \int_{\partial D} H(\mathbf{x},\mathbf{x}')T(\mathbf{x}')d\mathbf{x}' + f_i^{I0}(\mathbf{x})T_i^{I0*} + f_{ip}^{I1}(\mathbf{x})T_{ip}^{I1*} + \cdots \end{aligned} \tag{20}$$

where $H = KG_{,i'}(\mathbf{x},\mathbf{x}')n_i(\mathbf{x}')$ is the second fundamental solution of the thermal problem; the identities $G_{,i} = -G_{,i'}$ and $H_{,i} = -H_{,i'}$ are applied, and $q = q_i n_i$ represents the heat flux across the interface. Subsequently, the temperature gradients can be derived through further partial differentiation as Eq. (21),

$$T_{,i}(\mathbf{x}) = \int_{\partial D} G_{,i}(\mathbf{x},\mathbf{x}')q(\mathbf{x}')d\mathbf{x}' - \int_{\partial D} H_{,i}(\mathbf{x},\mathbf{x}')T(\mathbf{x}')d\mathbf{x}' + f_{j,i}^{I0}T_j^{I0*} + f_{jp,i}^{I1}T_{jp}^{I1*} + \cdots \tag{21}$$

The equivalent inclusion condition in terms of heat flux can be explicitly written in any order of the polynomial term as follows:

$$\begin{aligned} K^0\left(T_{,i}(\mathbf{0}) - T_i^{I0*}\right) &= K^I T_{,i}(\mathbf{0}) \\ K^0\left(T_{,ir}(\mathbf{0}) - T_{ir}^{I1*}\right) &= K^I T_{,ir}(\mathbf{0}) \end{aligned} \tag{22}$$

which can be extended to higher-order terms straightforwardly. Therefore, the ETG terms can be determined, and the temperature field can be obtained from Eq. (20).

Case 2: iBEM for elastic problems

Combining the boundary integral equation of elastic Green's function and the disturbance from equivalent inclusions, the following elastic boundary integral equation can be formulated,

$$\begin{aligned} u_i(\mathbf{x}) &= \int_{\partial D} G_{ij}(\mathbf{x},\mathbf{x}')t_j(\mathbf{x}')d\mathbf{x}' - \int_{\partial D} H_{ij}(\mathbf{x},\mathbf{x}')u_j(\mathbf{x}')d\mathbf{x}' - \int_{D} G_{ij,m}(\mathbf{x},\mathbf{x}')\varepsilon_{kl}(\mathbf{x}')C_{jmkl}(\mathbf{x}')d\mathbf{x}' \\ &= \int_{\partial D} G_{ij}(\mathbf{x},\mathbf{x}')t_j(\mathbf{x}')d\mathbf{x}' - \int_{\partial D} H_{ij}(\mathbf{x},\mathbf{x}')u_j(\mathbf{x}')d\mathbf{x}' + g_{ikl}^{I0}\varepsilon_{kl}^{I0*} + g_{iklp}^{I1}\varepsilon_{klp}^{I1*} + g_{iklpq}^{I2}\varepsilon_{klpq}^{I2*} + \cdots \end{aligned} \tag{23}$$

where the conventional boundary integral equations are retained, and the Eshelby tensors $\boldsymbol{g}$ involve disturbances from inclusions. Subsequently, the strain field can be derived based on the constitutive law as Eq. (24),

$$\begin{aligned} \varepsilon_{ij}(\mathbf{x}) = &\int_{\partial D} \frac{1}{2}\left\{G_{mi,j}(\mathbf{x},\mathbf{x}') + G_{mj,i}(\mathbf{x},\mathbf{x}')\right\} t_m\left(\mathbf{x}'\right) d\mathbf{x}' - \int_{\partial D} \frac{1}{2}\left\{H_{mi,j}\left(\mathbf{x},\mathbf{x}'\right) + H_{mj,i}\left(\mathbf{x},\mathbf{x}'\right)\right\} u_m\left(\mathbf{x}'\right) d\mathbf{x}' \\ &+ S_{ijkl}^{I0}\varepsilon_{kl}^{I0*} + S_{ijklp}^{I1}\varepsilon_{klp}^{I1*} + \cdots \end{aligned} \tag{24}$$

where $S_{ijkl} = \frac{g_{ikl,j}+g_{jkl,i}}{2}$, $S_{ijklp} = \frac{g_{iklp,j}+g_{jklp,i}}{2}$. Following the same fashion, the equivalence can be established for each order of polynomial-form terms at the center of the particles,

$$\begin{aligned} C_{ijmn}^0\left(\varepsilon_{mn}(\mathbf{0}) - \varepsilon_{mn}^{I0*}\right) &= C_{ijmn}^I\varepsilon_{mn}(\mathbf{0}) \\ C_{ijmn}^0\left(\varepsilon_{mn,r}(\mathbf{0}) - \varepsilon_{mnr}^{I1*}\right) &= C_{ijmn}^I\varepsilon_{mn,r}(\mathbf{0}) \end{aligned} \tag{25}$$

Although higher accuracy can be achieved by introducing higher-order terms, such as quadratic ones, for simplicity, this section only presents linear terms, although the quadratic terms have been implemented in the iBEM code.

Case 3: iBEM for thermoelastic problems

Thanks to the thermoelastic Green's function, the thermal induced effects are involved through boundary integral equations of boundary responses and domain integrals of ETG as Eq. (19),

$$\begin{aligned} u_i(\mathbf{x}) = &\int_{\partial D} G_i(\mathbf{x},\mathbf{x}')q(\mathbf{x}')d\mathbf{x}' - \int_{\partial D} H_i(\mathbf{x},\mathbf{x}')T(\mathbf{x}')d\mathbf{x}' + \int_{\partial D} G_{ij}(\mathbf{x},\mathbf{x}')t_j(\mathbf{x}')d\mathbf{x}' \\ &- \int_{\partial D} H_{ij}(\mathbf{x},\mathbf{x}')u_j(\mathbf{x}')d\mathbf{x}' + \int_{\Omega_I} G_{i,k}(\mathbf{x},\mathbf{x}')T_k^*(\mathbf{x}')K(\mathbf{x}')\,d\mathbf{x}' + \int_{\Omega_I} G_{ij,m}(\mathbf{x},\mathbf{x}')\varepsilon_{kl}^*(\mathbf{x}')C_{jmkl}(\mathbf{x}')\,d\mathbf{x}' \\ = &\int_{\partial D} G_i(\mathbf{x},\mathbf{x}')q(\mathbf{x}')d\mathbf{x}' - \int_{\partial D} H_i(\mathbf{x},\mathbf{x}')T(\mathbf{x}')d\mathbf{x}' + \int_{\partial D} G_{ij}(\mathbf{x},\mathbf{x}')t_j(\mathbf{x}')d\mathbf{x}' \\ &- \int_{\partial D} H_{ij}(\mathbf{x},\mathbf{x}')u_j(\mathbf{x}')d\mathbf{x}' + w_{ik}T_k^{I0*} + w_{ikp}T_{kp}^{I1*} + g_{ikl}\varepsilon_{kl}^{I0*} + g_{iklp}\varepsilon_{kl}^{I1*} \end{aligned} \tag{26}$$

where $H_i(\mathbf{x},\mathbf{x}') = K(\mathbf{x}')G_{i,j}(\mathbf{x},\mathbf{x}')n_j(\mathbf{x}')$; g_{iklpq} and w_{ikpq} have been defined in Eqs. (18) and (19), respectively. By employing the compatibility relationship, the mechanical strain at the interior point $\mathbf{x}$ can be derived:

$$\begin{aligned}\varepsilon_{ij}^{m}(\mathbf{x}) = &\int_{\partial D}\left\{G_{i,j}(\mathbf{x},\mathbf{x}')+G_{j,i}(\mathbf{x},\mathbf{x}')\right\}q(\mathbf{x}')d\mathbf{x}' - \int_{\partial D}\left\{H_{i,j}(\mathbf{x},\mathbf{x}')+H_{j,i}(\mathbf{x},\mathbf{x}')\right\}T(\mathbf{x}')d\mathbf{x}'\\ &+\int_{\partial D}\frac{1}{2}\left\{G_{mi,j}(\mathbf{x},\mathbf{x}')+G_{mj,i}(\mathbf{x},\mathbf{x}')\right\}t_m\left(\mathbf{x}'\right)d\mathbf{x}' - \int_{\partial D}\frac{1}{2}\left\{H_{mi,j}\left(\mathbf{x},\mathbf{x}'\right)+H_{mj,i}\left(\mathbf{x},\mathbf{x}'\right)\right\}u_m\left(\mathbf{x}'\right)d\mathbf{x}'\\ &+\left\{R_{ijk}^{I0}T_k^{I0*}+R_{ijkp}^{I1}T_{kp}^{I1*}\right\}+\left\{S_{ijkl}^{I1}\varepsilon_{kl}^{I0*}+S_{ijklp}^{I1}\varepsilon_{klp}^{I1*}\right\}-\alpha\delta_{ij}\left\{f_k^{I0}T_k^{I0*}+f_{kp}^{I1}T_{kp}^{I1*}\right\}\end{aligned} \tag{27}$$

where $R_{ijk}=\frac{w_{ik,j}+w_{jk,i}}{2}$, $R_{ijkp}=\frac{w_{ikp,j}+w_{jkp,i}}{2}$ and $R_{ijkpq}=\frac{w_{ikpq,j}+w_{jkpq,i}}{2}$. The ETG terms can be determined in Eq. (22). The equivalent stress conditions for $\boldsymbol{\varepsilon}^m$ are expressed as follows:

$$\begin{aligned}&C_{ijkl}^{0}\left(\varepsilon_{kl}^{m}(\mathbf{0})-\varepsilon_{kl}^{I0*}\right)-\gamma^{0}T(\mathbf{0})\delta_{ij}=C_{ijkl}^{I}\varepsilon_{kl}(\mathbf{0})-\gamma^{1}T(\mathbf{0})\delta_{ij}\\ &C_{ijkl}^{0}\left(\varepsilon_{kl,r}^{m}(\mathbf{0})-\varepsilon_{klr}^{I1*}\right)-\gamma^{0}T_{,r}(\mathbf{0})\delta_{ij}=C_{ijkl}^{I}\varepsilon_{kl,r}(\mathbf{0})-\gamma^{1}T_{,r}(\mathbf{0})\delta_{ij}\end{aligned} \tag{28}$$

Note that the equivalent inclusion conditions in Eqs. (22), (25), and (28) can be extended to multiple inhomogeneities with the local coordinates set at the center of each inhomogeneity (Yin et al., 2022).

In micromechanics, thermal strain induced by temperature fluctuations is typically perceived as an eigenstrain. However, a common misconception is that the ETG generates a temperature modification over the entire domain, thereby leading to an eigenstrain across the whole domain, which subsequently results in the inefficiency of the thermoelastic solution. The thermoelastic Green's function directly deals with the strain caused by ETG through **R** tensors rather than an eigenstrain with **S** tensors as illustrated in Eq. (27). Therefore, the volume integral is confined to the inclusion only, which enables an analytical solution (Wu et al., 2023a).

Although only up to linear terms of eigen-fields are provided in the above formulation, we can easily extend to higher-order terms similarly. The iBEM code has been implemented with constant, linear, and quadratic terms (Yin et al., 2022), and the corresponding tensors can be obtained in Appendix.

4. Numerical demonstration and verification of the iBEM

The iBEM algorithm has been implemented by the C++ code for the simulation of many particles for thermal, elastic, and thermoelastic problems, which has been extended to other multiphysical problems (Song et al., 2015; Yin et al., 2022; Wu and Yin, 2021). Because the interaction between particles reduces with the particle's center-center distance (r) rapidly, a cut-off distance is chosen to accelerate the computational process while maintaining accuracy. This section will demonstrate the iBEM results, verify them with FEM results, and evaluate the effect of the cut-off distance on the convergence of the results.

4.1. Verification of the iBEM with FEM

To verify the aforementioned algorithm for thermoelastic problems, shown as Fig. 1, the beam is specified with dimensions $b \times h \times l = 0.025\ \text{m} \times 0.025\ \text{m} \times 0.050\ \text{m}$. One aluminum particle is embedded in the HDPE matrix with its center at (0.025, 0, 0) as 0.01% volume fraction, so the radius $a = 0.91$ mm.

To provide precise simulation of local fields around inhomogeneities by iBEM, the surface of the beam has been discretized into 4000 equal-sized quadrilateral elements, each with a length is 1.25 mm. For FEM, a total of 99,500 tetrahedral elements are used with element sizes of 0.2 mm within the inhomogeneity, 0.4 mm around the inhomogeneity, and up to 2 mm in the other areas.

Firstly, a steady state heat transfer is considered with the boundary conditions as follows: On the left side of $x_1 = 0$, displacement $u_1 = 0$ with $u_2(0, b/2, h/2) = u_3(0, b/2, h/2) = 0$, free shear stress $\sigma_{12} = \sigma_{13} = 0$, and all other sides with free traction ($\sigma_{ij}n_i = 0$) and insulated boundary ($q_i n_i = 0$) unless a temperature boundary condition is applied to the left (T_L), right (T_R), top (T_T), bottom (T_B) sides, as follows:

1. Uniform temperature change $\Delta T = T_L = T_R = T_T = T_B = 20$ K;
2. Uniform temperature gradient from the left to the right as $T_L = 0$ K, $T_R = 20$ K;
3. Uniform temperature gradient (thermal bending) from the bottom to the top as $T_B = 0$ K, $T_T = 20$ K;

In Case 1, Fig. 2 shows the displacement u_1, normal stress σ_{11} and σ_{22} along the centerline x_1 passing the center of particle ($x_2 = 0.0125, x_3 = 0.0125$). The curves labeled 'iBEM UNI', 'iBEM LIN', and 'iBEM QUA' represent approximations incorporating the uniform, linear, and quadratic terms of the ETG and eigenstrain, respectively. These results show very good agreement with those obtained by FEM, although the FEM cannot well catch the stress discontinuity of σ_{22} on the interface. Under this uniform temperature change with zero temperature gradient, the presence of inhomogeneity introduces discontinuities in the local fields surrounding the particle, which can be clearly explained by the discontinuous features of Eshelby's tensor across the particle surface. However, because the thermal strain on the inhomogeneity is uniform, the eigenstrain caused by the stiffness mismatch is also uniform for a single particle embedded in an infinite domain. Therefore, the higher-order terms of eigenstrain disappear, and the three curves of iBEM results almost overlap with each other.

Case 2 studies the effect of temperature gradient in the horizontal direction. Fig. 3 displays the temperature T, displacement u_1, normal stresses σ_{11} and σ_{22} along the centerline x_1. The results from the 'iBEM UNI', 'iBEM LIN', and 'iBEM QUA' models agree well with those obtained via FEM. Because the aluminum particles exhibit a much higher thermal conductivity than the HDPE matrix, the temperature variation in the particle is much lower than the matrix but linearly changes along x_1 direction, which leads to linearly distributed eigenstrain and stress on the inhomogeneity. Although 'iBEM UNI' uses a uniform eigenstrain, the difference among the three iBEM curves is fairly small because the linear temperature change plays a dominant role. From the insets, the local field on the inhomogeneity is clarified, and the 'iBEM LIN' and 'iBEM QUA' provide better comparisons with FEM. Indeed, the linear eigenstrain can capture the exact solution for a single particle in an infinite domain under a uniform heat flux in the far field (Wu et al., 2023a), so that the 'iBEM LIN and 'iBEM QUA' provide similar accuracy.

Fig. 4 shows Case 3 for the thermal bending due to the temperature gradient from the bottom to the top. The iBEM results of deflections and normal stresses are compared with those obtained by the FEM. Fig. 4(a) shows the deflection of the neutral axis of the beam, which is similar to

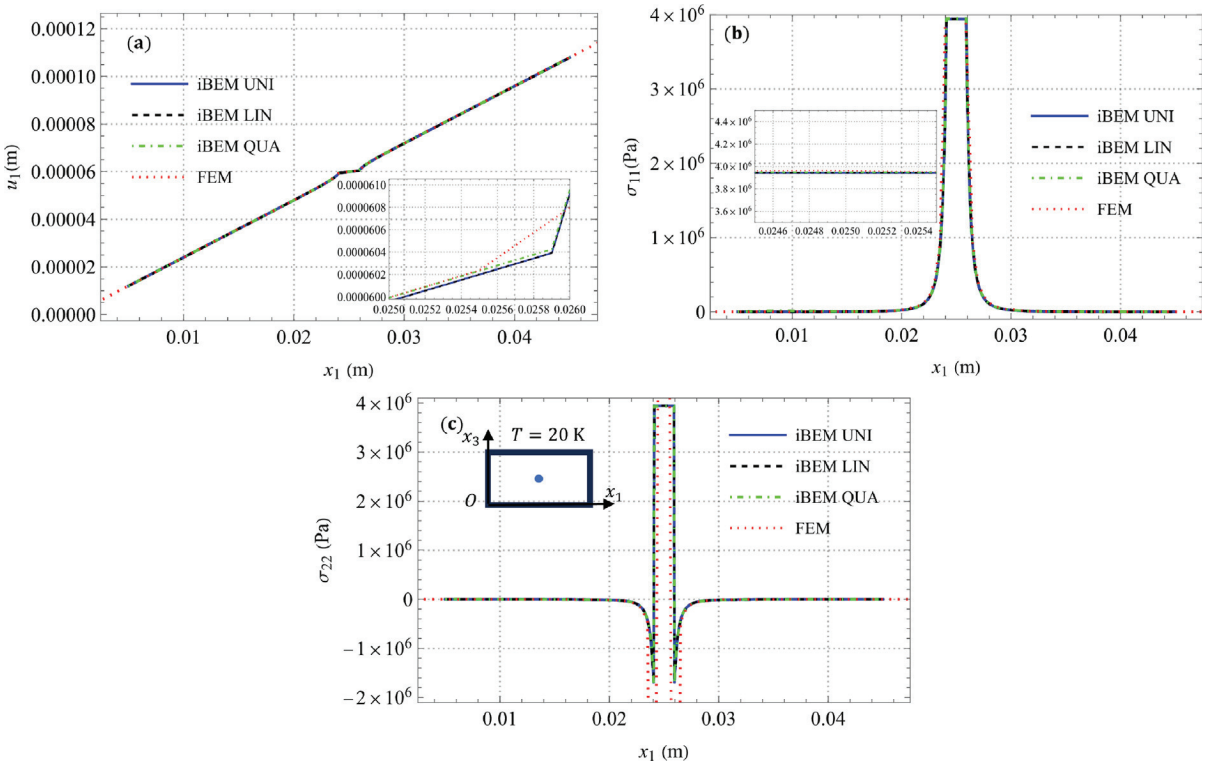

Fig. 2. Local fields of the beam under a uniform temperature change: (a) displacement u_1, (b) normal stress σ_{11}, and (c) σ_{22} along the centerline $x_1 \in [0.00, 0.05]$ m.

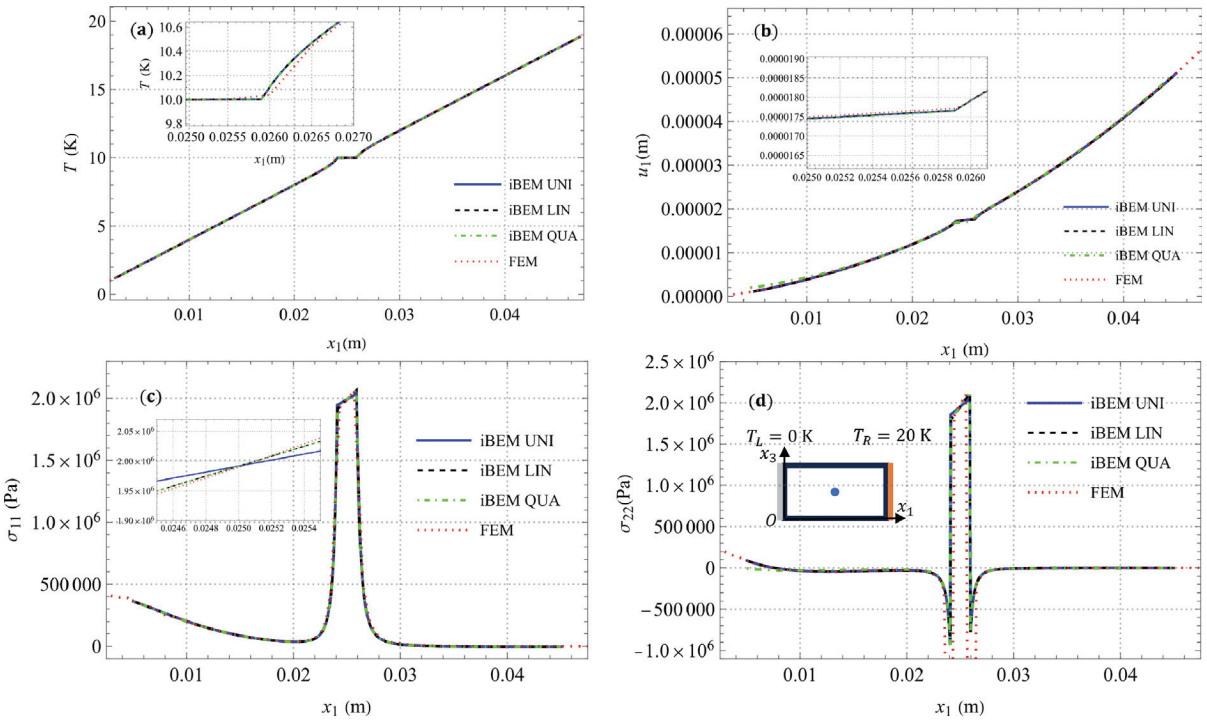

Fig. 3. Local fields of the beam under a horizontal temperature gradient: (a) temperature T, (b) displacement u_1, (c) normal stress σ_{11}, (d) normal stress σ_{22}, along the centerline $x_1 \in [0.00, 0.05]$ m.

the one caused by pure bending and shall produce a uniform stress in x_1 direction. However, due to the inhomogeneity, the stress significantly differs from the matrix.

Fig. 5 shows the stress and temperature changes in x_3 direction passing through the center of the particle at ($x_1 = 0.025, x_2 = 0.0125$). The stresses of σ_{11} and σ_{22} exhibit the same trend with very similar values, as the boundary effects of the four sides play a minor role on the stress along the central line in Fig. 5(a) and (b), respectively. In Fig. 5(c), temperature field T exhibits an approximately linear variation in the matrix

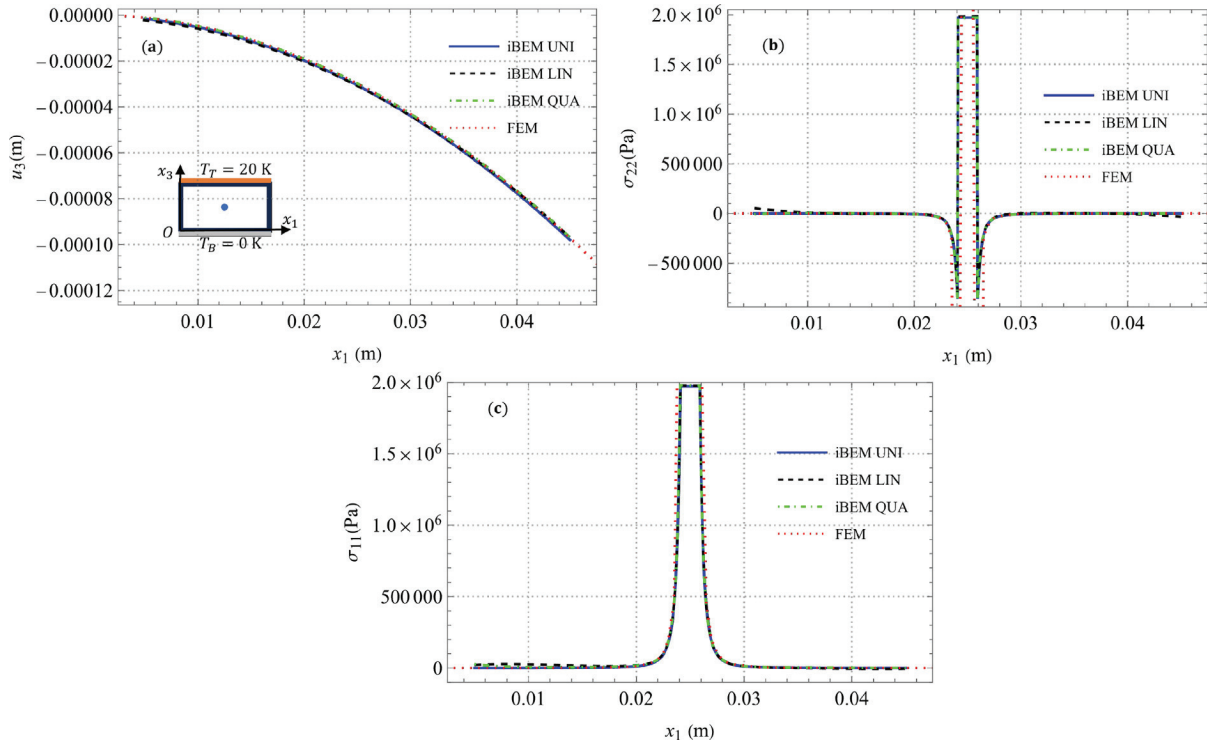

Fig. 4. Local fields along the centerline $x_1 \in [0.00, 0.05]$ m of the beam under thermal bending caused by a vertical temperature gradient: (a) deflection u_3, (b) normal stress σ_{22}, (c) normal stress σ_{11}.

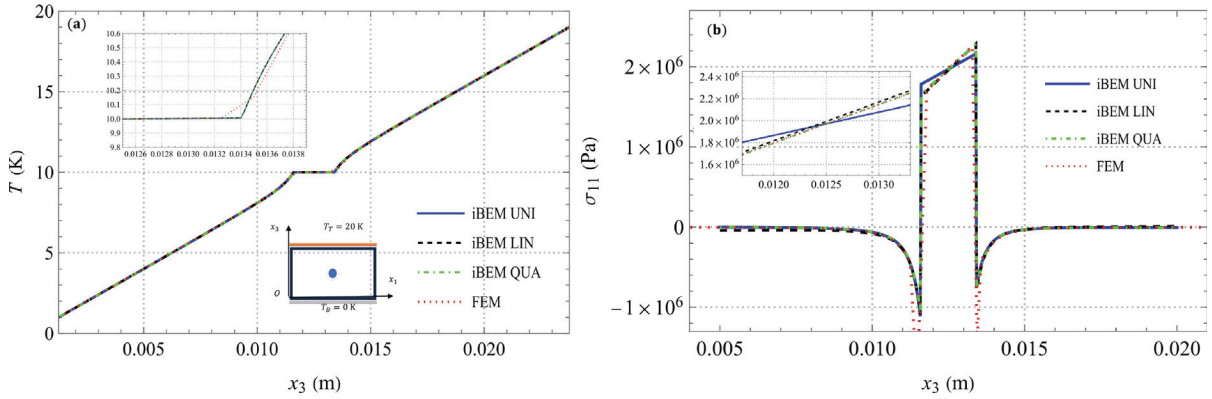

Fig. 5. Local fields along $x_3 \in [0.00, 0.025]$ m of the beam passing the particle center under thermal bending caused by a vertical temperature gradient: (a) Temperature T, (b) normal stress σ_{11}.

with very small variation in the particle due to its high thermal conductivity. Since both Case 2 and Case 3 investigate the effects of temperature gradients, Fig. 5(a), (b) and Fig. 3(b) exhibit similar patterns in terms of distribution and discontinuity. However, the variation of stress in the particle is much more uniform in 3(c) compared to Fig. 5(b), because the thermal bending creates a linearly distributed thermal strain in the matrix. 'iBEM LIN' and 'iBEM QUA' provide similar predictions, which fit the FEM results much better than the 'iBEM UNI'.

When a temperature difference is applied to two opposite boundary edges without the spherical particle, the temperature field should exhibit a linear distribution at the steady state. Due to the disturbance of the particle, specifically, the aluminum has much greater thermal conductivity than the HDPE, the variation of temperature within the particle is comparatively small in Fig. 3(a) and 5(a), which causes a nearly uniform thermal strain as well although a temperature gradient exists. For a uniform temperature change, the uniform eigenstrain with iBEM can provide accurate results, whereas a temperature gradient requires a linear eigenstrain in the iBEM. Particularly, the thermal bending of a beam exhibits a large linear eigenstrain, and the uniform eigenstrain cannot capture this feature and produces considerable errors in stress distribution. Verification by FEM demonstrates the accuracy, robustness, and efficiency of the modeling approach and provides flexibility in choosing the most suitable method for specific applications. Although 'iBEM QUA' provides the highest accuracy in general, 'iBEM LIN' offers comparable accuracy for the present thermoelastic behavior but faster computing speed. 'iBEM UNI' still provides good accuracy in the matrix with the fastest speed. When many particles are simulated for effective thermoelastic behavior, 'iBEM UNI' provides an advantage. However, the three orders of eigenstrains can be used together in one simulation of a many-particle system: uniform eigenstrain for particles in the central region and linear or quadratic eigenstrain for particles in the boundary region.

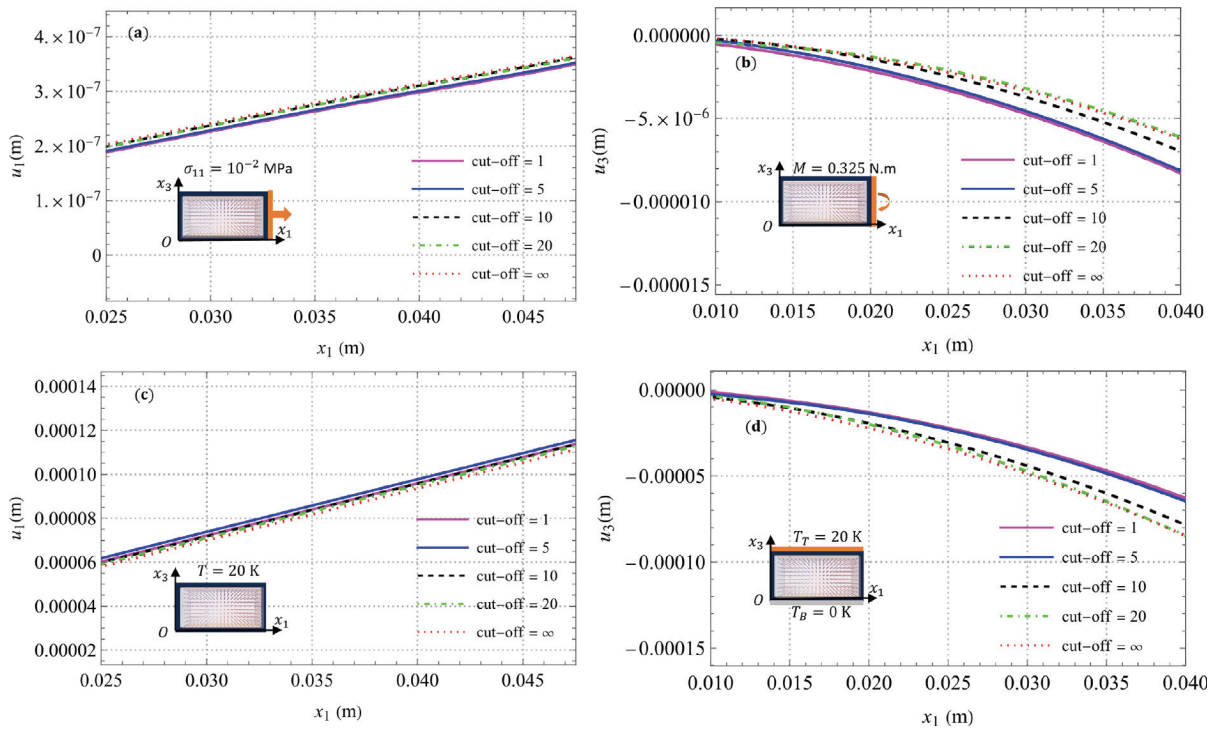

Fig. 6. Comparative analysis of five distinct cut-off ratios $(1, 5, 10, 20, \infty)$ across four different scenarios with the volume fraction $\phi = 1\%$: (a) displacement u_1 resulting from uniaxial loading, (b) deflection u_3 caused by pure bending, (c) displacement u_1 due to uniform temperature change, and (d) deflection u_3 arising from thermal bending.

4.2. The effect of cut-off ratio for particle interactions

When many particles are considered, the equivalent inclusion conditions in Eqs. (22), (25), and (28) will be expanded to all particles, leading to a time-consuming process to construct and solve the large linear equation system for the eigen-fields (Wu and Yin, 2021; Wu et al., 2022). Green's function describes the response at a field point caused by the excitation at a source point. As mentioned in Section 2, the thermal and elastic Green's function exhibits a decaying factor r^{-1}, which leads to the heat flux and stress caused by the ETG and eigenstrain, respectively, decaying with the distance at r^{-3}. Therefore, the effect of the long-range particle interaction rapidly decays with the increase of r. We have used a cut-off distance, which leads to a significant increase in the computational speed without loss of convergence of the results. According to the decaying feature of Green's function, the cut-off ratio is defined as the distance between the field point and the center of the particle and the characteristic length of the particle. For spherical particles, the characteristic length is the radius, and $\rho = r/a \in (15, 20)$ has been used to accelerate the computation without considerable loss of accuracy (Wu et al., 2022, 2023b). However, for thermoelastic Green's function, the decaying factor of stress is one order higher at r^{-2}, so that the convergence of the results is open to question when a cut-off ratio is applied to form the linear equation system.

This section conducts a numerical analysis of the effects of the cut-off ratio, which aims at a balance of computational efficiency and accuracy. Four cut-off ratios are investigated as $1, 5, 10$, and 20 in the following. In addition, when no cut-off is applied, we use cut-off $= \infty$ to represent it. To ease reproducing the results, 2000 inhomogeneities are uniformly distributed within the composite beam with the volume fraction $\phi = 1\%$ forming a simple cubic lattice. In this specific scenario, the radius of the particles is set at $a = 0.00033$ m, with the shortest distance between a particle and the boundary being $d_e = 0.00125$ m, and the minimum distance between particles being $d_p = 0.0025$ m. The parameter ρ defines the level of interaction: at $\rho = 1$, no particle interaction or boundary effect is considered in the linear equation system because of $r = a \times \rho < d_e < d_p$; at $\rho = 5$, so $d_e < r < d_p$, so only interactions between the nearest particles and boundary elements are considered, and the internal particle–particle interactions are disregarded; at $\rho \geq 10$, $d_p < r$, both particle interactions and boundary effects are considered with a certain region around each particle; and at $\rho = \infty$, full interaction among all particles and boundary elements is taken into account.

Fig. 6(a) shows uniaxial loading, in which the elastic boundary conditions are considered without temperature variation: (i) constrained displacement at the surface $x_1 = 0$; (ii) uniaxial load at the surface $x_1 = l = 0.05$ m with pressure 10^{-2} MPa and; (iii) all side surfaces are free of traction. Fig. 6(b) displays the pure bending test, applying identical elastic boundary conditions and a bending moment of 0.325 N/m. The cases of uniform temperature change and thermal bending are shown in Fig. 6(c) and (d), respectively, with the same boundary conditions and loadings as detailed in Figs. 2 and 4.

Fig. 6(a) and (c) show the comparison of the displacements u_1 along the centerline $x_1 \in [0.025, 0.05]$ m. The displacement u_1 within the range $x_1 \in [0.0, 0.025]$ m follows a similar trend and diminishes to 0 at the end of the beam. In a comparison of the four cases of the cut-off with the case without cut-off, they are very close to each other, although the case of cut-off= 20 and ∞ are almost overlapped. Long-range particle interactions play a minor role in the displacement field. Note that the eigenstrain in both cases is uniform for a single particle in an infinite matrix.

On the other hand, Fig. 6(b) and (d) plot the variation of deflection u_3 when $x_1 \in [0.010, 0.040]$ m. Greater discrepancies can be observed between curves of cut-off= $1, 5, 10$ and ∞; while the difference between curves with 20 and ∞ becomes negligible. Note that the eigenstrain in these cases is linearly distributed for a single particle in an infinite matrix. In addition, the boundary effects can also accumulate as the distance from the fix-end ($x_1 = 0$) becomes smaller. Although local fields near the boundary are sensitive to the cut-off ratio, the cut-off ratio strategy works well for the internal aspects. Therefore, careful consideration is demanded when involving intensive boundary effects.

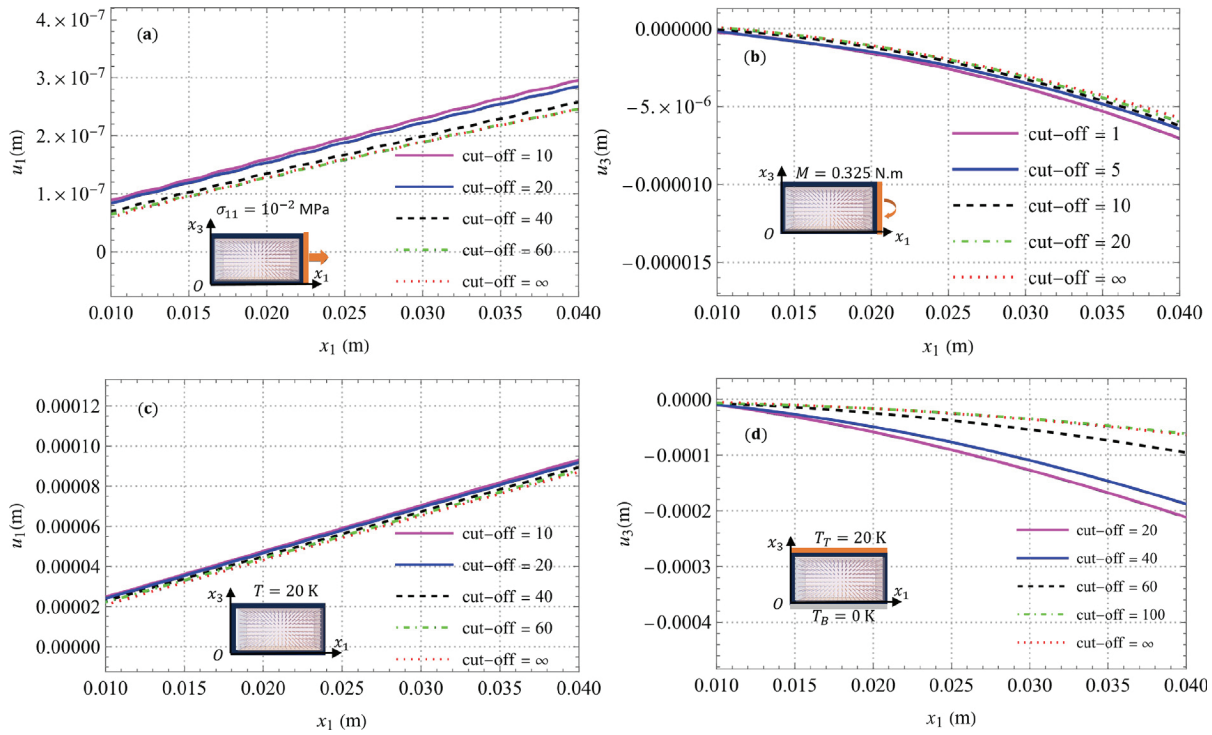

Fig. 7. Comparative analysis of distinct cut-off ratios across four different scenarios for the volume fraction $\phi = 10\%$: (a) displacement u_1 resulting from uniaxial loading, (b) deflection u_3 caused by pure bending, (c) displacement u_1 due to uniform temperature change, and (d) deflection u_3 arising from thermal bending.

When the volume fraction ϕ increases, the relative distance between particles decreases, the particle interactions will further increase the variation of eigenstrain in the particles, and a higher cut-off is required to reach a convergent $\phi = 10\%$, Fig. 7 shows the four cases of cut-off, where the increased radius of the particles, while preserving the same spacing between their centers as in the 2000 particle setup, effectively reduces the actual distance between the particles. So, this increase in particle size results in a heightened level of interaction among the particles. Fig. 7(a), (b), and (c) confirm that a cut-off ratio of 20 is appropriate for uniaxial loading, pure bending, and uniform temperature change, as anticipated. However, Fig. 7(d) reveals that in the case of thermal bending, a substantially higher cut-off ratio= 100 is used to ensure the convergence, which indeed takes into account most particles. It reveals that the thermoelastic Green's function with one order lower singularity leads to higher long-range particle interaction. Therefore, no cut-off shall be used unless the particle interactions are negligible for dilute composites such as $\phi = 1\%$ in Fig. 6.

5. Size effects of a composite beam under thermoelastic loading

After the iBEM algorithm is verified, we can use it to study the effects of SPR under different loading conditions. Given a volume fraction of particles in a specimen with the geometric dimension, a larger number of identical particles will be used with the decrease of particle size. From the uniform loading condition, the effective stiffness and CTE can be calculated. When the specimen is subjected to a pure bending or thermal bending, the deflection can be calculated from the actual heterogeneous specimen and the homogenized specimen, respectively. The difference can show the size effect on the applicability of the micromechanics convention.

5.1. Case 1: Uniaxial tensile loading

This subsection aims to investigate the size effects on the effective modulus, Young's modulus, and Poisson's ratio of the composite beam. To control microstructural effects, such as different distributions, the composite beam is evenly divided into $16 \times s^3$ sub-cells, where s refers to the number of divisions along the x_1 direction. Each equal-sized spherical particle is located at the center of each sub-cell, and the number of particles can be modified by changing the radius of the particles. Similarly to the previous work (Wu and Yin, 2021), the effective moduli are evaluated through uniaxial loading applied at the surface ($x_1 = l$) and constrained longitudinal displacement at the surface ($x_1 = 0$). The effective moduli can be calculated by averaging the displacements at the surface ($x_1 = l = 0.05$ m) and the lateral surfaces.

Fig. 8(a) and (b) show the variations of effective Young's modulus and Poisson's ratio with particles of decreasing radius. When the number of particles starts to increase, the effective moduli change accordingly. For example, when the volume fraction is equal to 10%, the effective Young's modulus slowly increases from 1.45 GPa to 1.49 GPa, and the effective Poisson's ratio fluctuates around the value 0.44. A similar trend can be observed when the volume fraction equals 30%. When the number of particles reaches 16,000, the microstructure of the composite beam becomes sufficiently refined; as a result, the results converge to the constants. As the volume fraction rises from 10% to 30%, there is a noticeable development of a peak. For the 10% volume fraction, a subtle peak at 1024 particles was detected. With 2000 particles, this value slightly decreased to 1.39×10^9 and then showed subtle fluctuations around 1.40×10^9.

Due to the symmetric distribution of inhomogeneities, the local stress fields are also periodic, following the symmetric mechanical load along the x_1 direction. Fig. 9(a) and (b) present a symmetric distribution of normal stress σ_{11} and σ_{22}, respectively. As the size of the particles decreases, there is a corresponding slight reduction in the amplitude of the local stress fields.

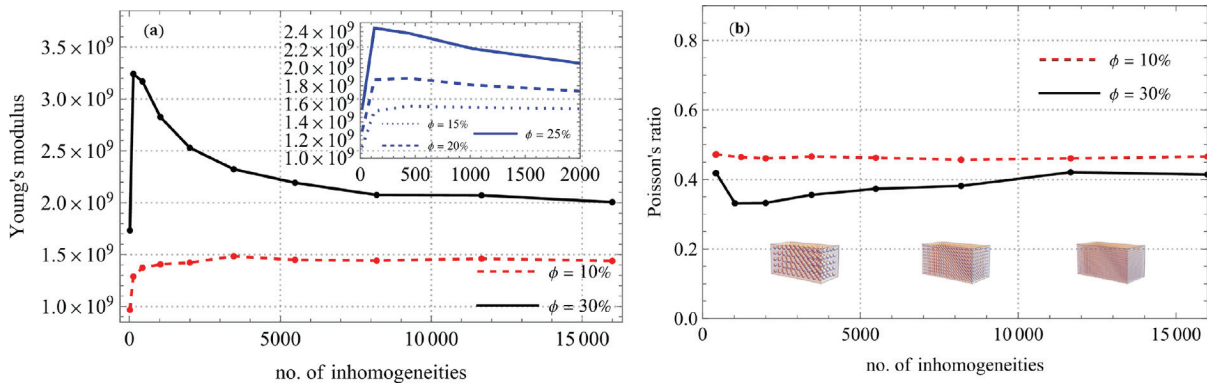

Fig. 8. Effective elastic properties: (a) Young's modulus and (b) Poisson's ratio calculated from the composite beam with 10% and 30% volume fractions under uniaxial load, embedded with $2\times(2n)^3$ (n = 1, 2, …,10) spherical particles.

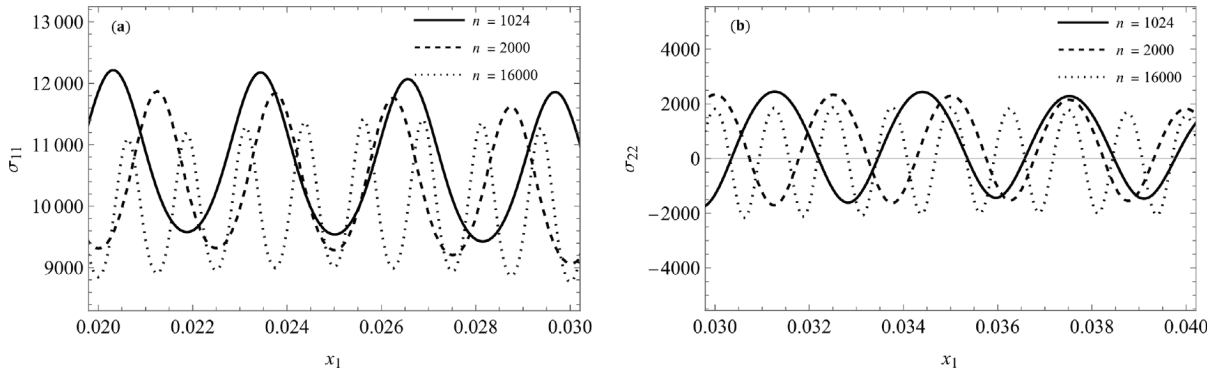

Fig. 9. Variation of normal stresses along the centerline x_1 when the number of particles is 1024,2000 or 16,000 with the volume fraction $\phi = 10\%$ for (a) σ_{11} and (b) σ_{22}.

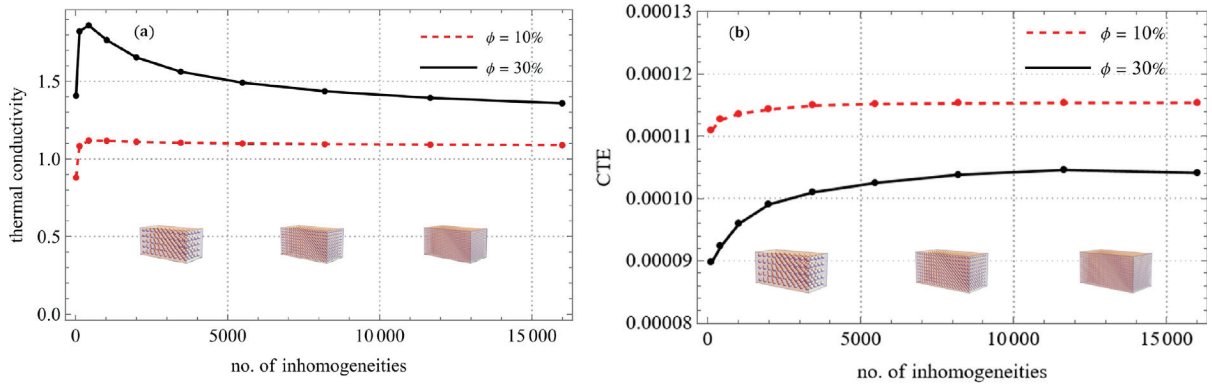

Fig. 10. Effective thermomechanical properties: (a) thermal conductivity calculated under uniform temperature gradient and (b) CTE calculated under uniform temperature change from the composite beam with 10% and 30% volume fractions, embedded with $16\times n^2$ (n = 1, 2, …,10) spherical particles.

5.2. Case 2: uniform temperature boundary condition

This subsection investigates the size effects on effective thermal conductivity and the CTE. Following the same fashion as the elastic test of the preceding subsection, to control the effect of microstructures, the inhomogeneities are evenly distributed. Effective thermal conductivity and CTE are determined by applying uniform temperature boundary conditions. For effective thermal conductivity, a uniform temperature gradient is simulated using a uniform heat flux. Meanwhile, under a uniform temperature change with no temperature gradient, the resulting uniform thermal expansion from a temperature change ΔT facilitates the measurement of CTE across the entire beam. Fig. 10(a) and (b) plot the variation of thermal conductivity and CTE versus the number of inhomogeneities, respectively. Similar trends can be observed in both figures: when the number of inhomogeneities is large enough, say 12,000, the effective thermal properties converge. Compared to Fig. 8(a) and (b), composites with smaller volume fractions show a more rapid convergent trend, and the effective thermal properties require a greater number of inhomogeneities to obtain a convergent solution (from 8000 to 12,000). Such a phenomenon can be explained as different decaying factors of the Green's function. For example, elastic Green's function for interior stress decays as r^{-3} while thermoelastic Green's function for interior stress decays as r^{-1}.

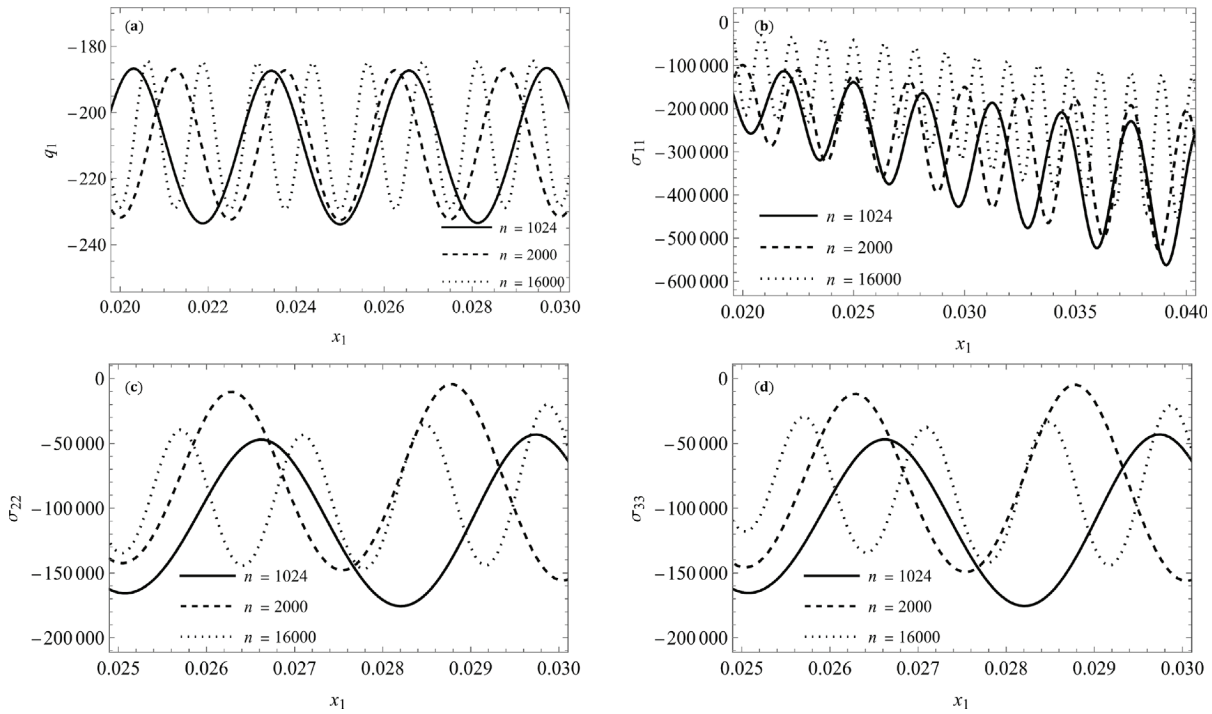

Fig. 11. Variation of thermomechanical local fields along the centerline $x_1 \in [0.02, 0.03]$ m when the number of particles is 1024,2000 and 16,000 with the volume fraction $\phi = 10\%$, (a) heat flux q_1, (b) normal stress σ_{11}, (c) normal stress σ_{22} and (d) normal stress σ_{33}.

Fig. 11(a–d) shows the local thermomechanical fields along the centerline $x_1 \in [0.02, 0.03]$ m when the volume fraction is 10%. As indicated in Fig. 11(a), when the number of inhomogeneities increases, the amplitude of the heat flux does not change obviously, which can be interpreted as a consequence caused by the uniform thermal boundary condition. Fig. 11(b) shows that although the overall amplitude of σ_{11} changes slightly with the number of inhomogeneities, the maximum thermal stress decreases for smaller inhomogeneities.

6. Virtual experiments of composite beams versus the homogenized beams

Considering the different size effects on beam bending, we conduct virtual experiments of composite beams with spherical inhomogeneities in comparison to the homogeneous beam with the elastic constants and CTE obtained by the homogenization with uniform testing load.

6.1. Deflection of pure bending

When a beam is subjected to pure bending, a linear stress field will be induced with a constant curvature for the deformation. However, when many inhomogeneities are embedded in a composite beam, the local field is highly disturbed by the material mismatch. With the increase of the SPR, the deflection converges to a constant value as it achieves a refined microstructure state.

By keeping the volume fraction $\phi = 10\%$ with the same dimension of the beam, increasing the number of inhomogeneities from 128 to 2000 will lead to the reduction of the particle diameter to 40%. Interestingly, the effective Young's modulus of the beam remains the similar value obtained by uniaxial loading, but the deflection of the composite beam may change considerably.

Fig. 12 shows how deflection varies under pure bending for the heterogeneous and homogeneous beams, following the same boundary conditions and loading as in Fig. 7(b). In the homogeneous beam with the effective Young's modulus, because the simulations are based on the effective Young's modulus, the difference of deflection between three particle sizes is slight, suggesting that size effects are negligible in this SPR range. In contrast, there is a sharp decrease in deflection in the heterogeneous case, from -1.5×10^{-5} m to -0.5×10^{-5} m, highlighting the significance of size effects. However, when the particle number reaches 2000, the composite beam converges to the three cases of the homogeneous beam, and the size effects can be disregarded. This figure illustrates when SPR = 6.95 the uniaxial loading can provide a convergent result for effective material behavior. However, this critical SPR is not applicable to the pure bending, but SPR = 17.36 is required to achieve the convergent result.

The above discovery imposes a challenge for the applicability of the homogenization-based micromechanical method. When SPR is small or moderate, the effect of the actual microstructure cannot be taken lightly, particularly under non-uniform loading conditions. A detailed analysis considering the actual microstructures is necessary.

6.2. Deflection in thermal bending with a temperature gradient along the thickness

Similarly, thermal bending can be considered with a temperature gradient along the thickness. For the homogenized beam with the CTE and Young's modulus obtained by a uniform temperature and a uniaxial loading, respectively, a few particles are enough to generate the convergent result of the deflection curve. However, the actual heterogeneous beam with the same number of particles may yield a much different result from the homogenized beam.

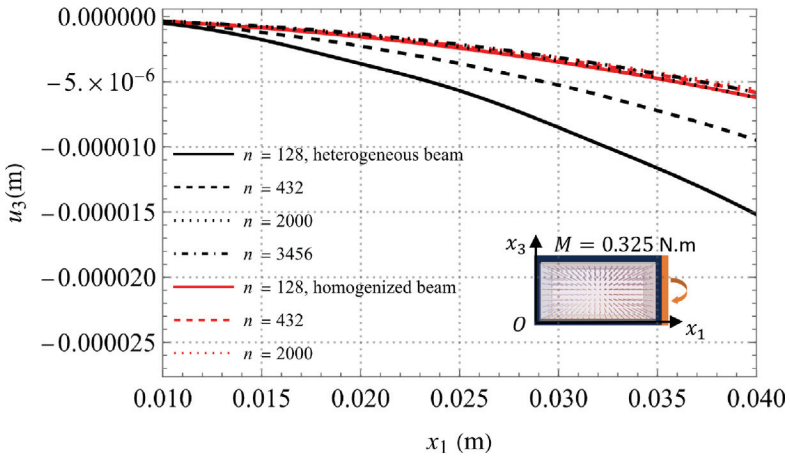

Fig. 12. Variation of deflection u_3 vs. the centerline $x_1 \in [0.01, 0.04]$ m under pure bending with the volume fraction $\phi = 10\%$ for 128, 432, 2000, and 3456 particles.

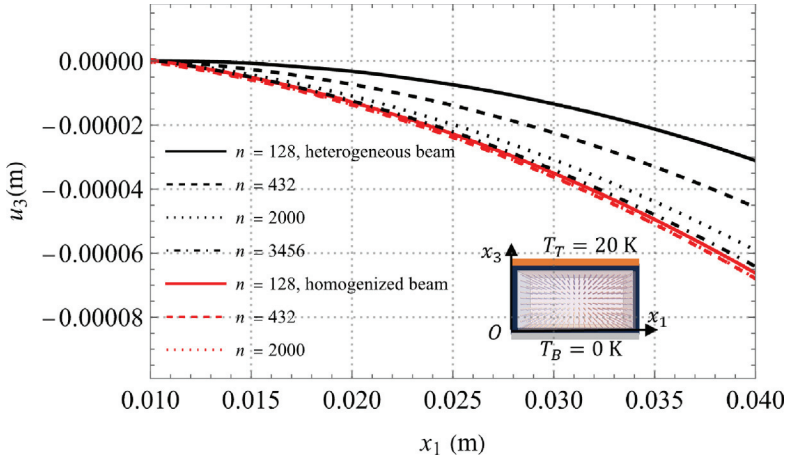

Fig. 13. Variation of deflection u_3 vs. the centerline $x_1 \in [0.01, 0.04]$ m under thermal bending with the volume fraction $\phi = 10\%$ for 128, 432, 2000, and 3456 particles.

Fig. 13 shows the deflection of the beam under thermal bending, consistent with the settings in Fig. 7(d). Interestingly, increasing the number of particles leads to greater deflection in thermal bending until a convergent result is obtained, which is opposite to the trend that observed in pure bending. As for pure bending, more particles are located at the surface edge, higher flexural rigidity can be reached, so smaller deflection is observed.

In the homogeneous case, based on the effective material constants obtained by the three cases of 128, 432, 2000, and 3456 particles, very similar deflection curves are obtained, which means that SPR = 20.84 yields the convergent result. However, for heterogeneous composite beam, much higher SPR is required to reach the convergent result.

The heterogeneous case shows a substantial increase in deflection, in which the maximum deflection moves from -0.3×10^{-4} m for $n = 126$ to -0.6×10^{-4} m for $n = 3456$.

Overall, Figs. 12 and 13 show the convergence of deflection in both pure bending and thermal cases through the virtual experiments by the iBEM for beams with different SPRs. Although a small SPR can provide convergent CTE and Young's modulus, the heterogeneous composite beams exhibit significantly different behavior from the corresponding homogenized beams under beam bending.

7. Conclusions

Conventional micromechanics approaches have utilized large RVEs under uniform loads to determine the effective elastic moduli for modeling the structural behavior of particulate composites. However, two issues limit the applicability of micromechanical models: firstly, the actual stress states exhibit stress variations, such as a linear change in pure bending of beams, which are not taken into account in the homogenization models under uniform loads; secondly, the size of the structure members may not be large enough, making it challenging to achieve convergent effective stiffness values that simultaneously consider particle size and beam length. As a result, the effects of particle size significantly influence the overall structural behavior. The paper uses iBEM to simulate the thermoelastic behavior of many aluminum particles filled in an HDPE matrix with a periodic distribution with the following highlights:

1. For a volume fraction of 10%, although 432 particles (SPR = 6.95) are enough to obtain convergent elastic constants and thermal expansion coefficient, 2000 and 12,000 particles (SPR = 17.36 and 20.84) are required to reach a convergent solution for pure and thermal bending, respectively;

2. The thermoelastic Green's function exhibits one order lower singularity than thermal or elastic Green's functions, which leads to the divergence of the volume integral in composites with a high volume fraction of particles. The homogenization for thermoelastic problems may not always be applicable, and an actual heterogeneous material system should be used;
3. Although the iBEM is much faster than FEM, it may still require significant computational resources, especially when dealing with complex geometries or large datasets. The cut-off of particle interactions can significantly save computational cost, but the accuracy changes with particle size and problem type.
4. When the volume fraction of particles is small, such as 1%, or a single small particle is embedded in the matrix, the particle interactions or boundary effects play a minor role, and the higher-order terms of eigen-fields in the iBEM can be disregarded; whereas for high volume fractions, such as 30%, higher-order terms of eigen-fields are required.
5. For a small or moderate SPR, the conventional homogenization method with a uniform test loading may not be applicable to predict the material behavior under non-uniform loading conditions. The actual microstructure shall be used for simulation and modeling.

The iBEM can be a powerful tool to simulate actual material samples for digital twins through virtual experiments of the materials in parallel to the physical material testing or actual loading.

CRediT authorship contribution statement

Jinming Zhang: Data curation, Methodology, Software, Validation, Visualization, Writing – original draft. **Chunlin Wu:** Conceptualization, Methodology, Software, Writing – review & editing. **Huiming Yin:** Conceptualization, Funding acquisition, Resources, Supervision, Writing – review & editing.

Declaration of competing interest

The authors declare that they have no known competing financial interests or personal relationships that could have appeared to influence the work reported in this paper.

Data availability

Data will be made available on request.

Acknowledgments

This work is sponsored by the National Science Foundation IIP #1941244, U.S. Department of Agriculture NIFA #2021-67021-34201, Natural Science Foundational of China No. 12302086, Pao Family Memorial Fellowship and the Chenguang Program No. 23CGA50 of Shanghai Education Development Foundation and Shanghai Municipal Education Commission, whose support is gratefully acknowledged.

Appendix. Explicit form of Eshelby's tensor of spherical inclusion

Let r denote the distance between field and source points, $r = |\mathbf{x} - \mathbf{x}^{Ic}|$ and r_i represent its ith component.

A.1. The integrals of harmonic potential

$$\boldsymbol{\Phi} = 2\pi \begin{cases} a^2 - \frac{r^2}{3} & a \geq r \\ \frac{2a^3}{3r} & a < r \end{cases} \tag{A.1}$$

$$\boldsymbol{\Phi}_n = \frac{2\pi}{15} \begin{cases} \left(5a^2 - 3r^2\right) r_n & a \geq r \\ \frac{2a^5 r_n}{r^3} & a < r \end{cases} \tag{A.2}$$

$$\boldsymbol{\Phi}_{mn} = \frac{\pi}{315} \begin{cases} (105a^4 - 42a^2r^2 + 9r^4)\delta_{mn} + (90a^2 - 70r^2)r_m r_n & a \geq r \\ \frac{4}{r^7}(-3a^5r^4(a^2 - 7r^2)\delta_{mn} + 5a^7 r_m r_n) & a < r \end{cases} \tag{A.3}$$

$$\boldsymbol{\Phi}_{,i} = \frac{4\pi}{3} \begin{cases} -r_i & a \geq r \\ -\frac{a^3 r_i}{r^3} & a < r \end{cases} \tag{A.4}$$

$$\boldsymbol{\Phi}_{n,i} = \frac{2\pi}{15} \begin{cases} (5a^2 - 3r^2)\delta_{in} - 6r_i r_n & a \geq r \\ \frac{2a^5}{r^5}(r^2\delta_{in} - 3r_i r_n) & a < r \end{cases} \tag{A.5}$$

$$\boldsymbol{\Phi}_{mn,i} = \frac{2\pi}{105} \begin{cases} 3(7a^2 - 5r^2)(\delta_{in}r_m + \delta_{im}r_n) - 2(7a^2 - 3r^2)\delta_{mn}r_i + 15r_m r_n r_i & a \geq r \\ \frac{2a^5}{r^7}[3a^2r^2(\delta_{in}r_m + \delta_{im}r_n) + r^2(3a^2 - 7r^2)\delta_{mn}r_i - 15a^2 r_m r_n r_i] & a < r \end{cases} \tag{A.6}$$

$$\boldsymbol{\Phi}_{,ij} = \frac{4\pi}{3} \begin{cases} -\delta_{ij} & a \geq r \\ -a^3(\frac{\delta_{ij}}{r^3} - \frac{3r_i r_j}{r^5}) & a < r \end{cases} \tag{A.7}$$

$$\boldsymbol{\Phi}_{n,ij} = \frac{2\pi}{15} \begin{cases} -6(r_i\delta_{jn} + r_j\delta_{in} + r_n\delta_{ij}) & a \geq r \\ \frac{-2a^5 r_j}{r^7}(r^2\delta_{in} - 3r_i r_n) + \frac{2a^5}{r^5}(2r_j\delta_{in} - 3r_i\delta_{jn} - 3\delta_{in}r_n) & a < r \end{cases} \tag{A.8}$$

$$\Phi_{mn,ij} = \frac{2\pi}{105}\begin{cases}(-30r_j)(\delta_{in}r_m+\delta_{im}r_n)+(21a^2-15r^2)(\delta_{in}\delta_{mj}+\delta_{im}\delta_{nj})+12r_j\delta_{mn}r_i \\ -(14a^2-6r^2)\delta_{mn}\delta_{ij}+15(\delta_{mj}r_nr_i+\delta_{nj}r_mr_i+\delta_{ij}r_mr_n) & a\geq r \\ 2a^5[\frac{-15a^2}{r^7}(\delta_{in}r_m+\delta_{im}r_n+\delta_{mn}r_i)+\frac{3a^2}{r^5}(\delta_{in}\delta_{mj}+\delta_{im}\delta_{nj}+\delta_{mn}\delta_{ij}) \\ +\frac{21}{r^5}\delta_{mn}r_i+\frac{-7}{r^3}\delta_{mn}\delta_{ij}+\frac{105a^2}{r^9}r_mr_nr_i-\frac{15a^2}{r^7}(\delta_{mj}r_nr_i+\delta_{nj}r_mr_i+\delta_{ij}r_mr_n)] & a<r\end{cases} \tag{A.9}$$

A.2. The integrals of biharmonic potential

$$\Psi_{,i} = \frac{4\pi}{15}\begin{cases}(5a^2-r^2)r_i & a\geq r \\ -\frac{r_i}{r^3}(a^5-5a^3r^2) & a<r\end{cases} \tag{A.10}$$

$$\Psi_{n,i} = \frac{\pi}{105}\begin{cases}(-35a^4+14a^2r^2-3r^4)\delta_{in}+4(7a^2-3r^2)r_ir_n & a\geq r \\ \frac{4a^5}{r^5}[r^2(a^2-7r^2)\delta_{in}+(-3a^2+7r^2)r_ir_n] & a<r\end{cases} \tag{A.11}$$

$$\Psi_{mn,i} = \frac{\pi}{315}\begin{cases}-(21a^4-18a^2r^2+5r^4)(\delta_{in}r_m+\delta_{im}r_n) \\ +4(21a^4-6a^2r^2+r^4)\delta_{mn}r_i+(9a^2-5r^2)r_mr_nr_i & a\geq r \\ \frac{4a^5}{r^7}[a^2r^2(a^2-3r^2)(\delta_{in}r_m+\delta_{im}r_n) \\ +r^2(a^4-6a^2r^2+21r^4)\delta_{mn}r_i+a^2(-5a^2+9r^2)r_mr_nr_i] & a<r\end{cases} \tag{A.12}$$

$$\Psi_{,ij} = \frac{4\pi}{15}\begin{cases}(5a^2-r^2)\delta_{ij}-2r_ir_j & a\geq r \\ \frac{a^3}{r^5}[r^2(-a^2+5r^2)\delta_{ij}+(3a^2-5r^2)r_ir_j] & a<r\end{cases} \tag{A.13}$$

$$\Psi_{n,ij} = \frac{4\pi}{105}\begin{cases}(7a^2-3r^2)(\delta_{in}r_j+\delta_{ij}r_n+\delta_{jn}r_i)-6r_ir_jr_n & a\geq r \\ \frac{a^5}{r^7}[r^2(-3a^2+7r^2)(\delta_{in}r_j+\delta_{ij}r_n+\delta_{jn}r_i)+3(5a^2-7r^2)r_ir_jr_n] & a<r\end{cases} \tag{A.14}$$

$$\Psi_{mn,ij} = \frac{\pi}{315}\begin{cases}(-21a^4+18a^2r^2-5r^4)(\delta_{im}\delta_{jn}+\delta_{in}\delta_{jm})+(84a^8-24a^6r^2+4a^4r^4)\delta_{ij}\delta_{mn} \\ +(36a^2-20r^2)\delta_{im}r_nr_j+4(9a^2-5r^2)(\delta_{in}r_mr_j+\delta_{ij}r_mr_n \\ +\delta_{im}r_jr_n+\delta_{jn}r_mr_i+\delta_{jm}r_nr_i)-16(3a^2-r^2)\delta_{mn}r_ir_j-40r_ir_jr_mr_n & a\geq r \\ \frac{4a^5}{r^9}\{r^4a^2[(a^2-3r^2)(\delta_{in}\delta_{jm}+\delta_{im}\delta_{jn})+a^2(a^4-6a^2r^2+21r^4)\delta_{ij}\delta_{mn}] \\ -r^2a^2(5a^2-9r^2)(\delta_{im}r_jr_n+\delta_{in}r_jr_m+\delta_{ij}r_nr_m+\delta_{jn}r_mr_i+\delta_{jm}r_nr_i) \\ +r^2(-5a^4+18a^2r^2-21r^4)\delta_{mn}r_ir_j+5a^2(7a^2-9r^2)r_ir_jr_mr_n\} & a<r\end{cases} \tag{A.15}$$

$$\Psi_{,ijk} = \frac{4\pi}{15}\begin{cases}-2(\delta_{jk}r_i+\delta_{ik}r_j+\delta_{ij}r_k) & a\geq r \\ \frac{a^3}{r^7}[r^2(3a^2-5r^2)(\delta_{ij}r_k+\delta_{ik}r_j+\delta_{jk}r_i)-15(a^2-r^2)r_ir_jr_k] & a<r\end{cases} \tag{A.16}$$

$$\Psi_{n,ijk} = \frac{4\pi}{105}\begin{cases}(7a^2-3r^2)(\delta_{in}\delta_{jk}+\delta_{ik}\delta_{jn}+\delta_{ij}\delta_{kn}) \\ -6(\delta_{jk}r_ir_n+\delta_{jn}r_i+\delta_{in}r_jr_k+\delta_{ij}r_nr_k+\delta_{kn}r_ir_j+\delta_{ik}r_nr_j) & a\geq r \\ \frac{1}{r^9}a^5[r^4(-3a^2+7r^2)(\delta_{in}\delta_{jk}+\delta_{ik}\delta_{jn}+\delta_{ij}\delta_{kn}) \\ +3r^2(5a^2-7r^2)(\delta_{ik}r_jr_n+\delta_{in}r_jr_k+\delta_{ij}r_nr_k+\delta_{jn}r_kr_i+\delta_{jk}r_ir_n+\delta_{kn}r_ir_j) \\ -105(a^2-r^2)r_ir_jr_kr_n] & a<r\end{cases} \tag{A.17}$$

$$\Psi_{mn,ijk} = \frac{4\pi}{315}\begin{cases}(9a^2-5r^2)(\delta_{jn}\delta_{km}r_i+\delta_{jm}\delta_{kn}r_i+\delta_{in}\delta_{jk}r_m+\delta_{ik}\delta_{jn}r_m+\delta_{ij}\delta_{kn}r_m \\ +\delta_{ij}\delta_{mn}r_n+\delta_{im}\delta_{kn}r_j+\delta_{in}\delta_{km}r_j+\delta_{in}\delta_{jm}r_k+\delta_{im}\delta_{jn}r_k) \\ -(12a^6-4a^4r^2)(\delta_{jk}\delta_{mn}r_i+\delta_{ik}\delta_{mn}r_j+\delta_{ij}\delta_{mn}r_k) \\ -10(\delta_{jk}r_ir_mr_n+\delta_{km}r_ir_jr_n+\delta_{kn}r_ir_jr_m+\delta_{ik}r_nr_jr_m \\ +\delta_{jn}r_kr_mr_i+\delta_{in}r_kr_mr_j+\delta_{ij}r_kr_mr_n+\delta_{jm}r_kr_ir_n+\delta_{im}r_nr_jr_k) \\ +8a^4\delta_{mn}r_ir_jr_k & a\geq r \\ \frac{a^7}{r^{11}}[r^4(-5a^2+9r^2)(\delta_{in}\delta_{jk}r_m+\delta_{ik}\delta_{jn}r_m+\delta_{ij}\delta_{kn}r_m+\delta_{im}\delta_{jk}r_n+\delta_{ik}\delta_{jm}r_n \\ +\delta_{ij}\delta_{km}r_n+\delta_{in}\delta_{km}r_j+\delta_{im}\delta_{kn}r_j+\delta_{in}\delta_{jm}r_k+\delta_{im}\delta_{jn}r_k+\delta_{jn}\delta_{km}r_i+\delta_{jm}\delta_{kn}r_i) \\ -r^4a^2(5a^4-18a^2r^2+21r^4)(\delta_{ik}\delta_{mn}r_j+\delta_{ij}\delta_{mn}r_k+\delta_{jk}\delta_{mn}r_i) \\ +5r^2(7a^2-9r^2)(\delta_{ik}r_mr_nr_j+\delta_{im}r_jr_nr_k+\delta_{in}r_jr_mr_k+\delta_{ij}r_nr_mr_k+\delta_{jm}r_kr_nr_i \\ +\delta_{jn}r_ir_kr_m+\delta_{jk}r_ir_nr_m+\delta_{kn}r_ir_jr_m+\delta_{km}r_ir_jr_n) \\ +a^2(35a^4-90a^2r^2+63r^4)\delta_{mn}r_ir_jr_k-315(a^2-r^2)r_mr_nr_ir_jr_k] & a<r\end{cases} \tag{A.18}$$

$$\Psi_{,ijkl} = \frac{4\pi}{15}\begin{cases}-2(\delta_{jk}\delta_{il}+\delta_{ik}\delta_{jl}+\delta_{ij}\delta_{kl}) & a\geq r \\ a^3[(\frac{-15a^2r_l}{r^7}-\frac{-15r_l}{r^5})(\delta_{ij}r_k+\delta_{ik}r_j+\delta_{jk}r_i) \\ +(-\frac{15a^2}{r^7}\frac{3a^2+15}{r^5}-\frac{5}{r^3})(\delta_{ij}\delta_{kl}+\delta_{ik}\delta_{jl}+\delta_{jk}\delta_{il})+(\frac{105a^2}{r^9}-\frac{75}{r^7})r_ir_jr_k] & a<r\end{cases} \tag{A.19}$$

Table A.2
Eshelby's tensors.

Term	Thermal	Thermoelastic
Uniform:	$f_i^{I0} = -\frac{\Phi_{,i}}{4\pi}$	$w_{ik}^{I0} = -\frac{\alpha^0}{8\pi}\frac{1+\nu^0}{1-\nu^0}\Psi_{,ik}$
Linear:	$f_{ik}^{I1} = -\frac{\Phi_{,ki}}{4\pi}$	$w_{ikp}^{I1} = -\frac{\alpha^0}{8\pi}\frac{1+\nu^0}{1-\nu^0}\Psi_{p,ik}$
Quadratic:	$f_{ikl}^{I2} = -\frac{\Phi_{,kli}}{4\pi}$	$w_{ikpq}^{I2} = -\frac{\alpha^0}{8\pi}\frac{1+\nu^0}{1-\nu^0}\Psi_{pq,ik}$
Elastic		
Uniform:	$g_{ikl}^{I0} = -(\frac{1}{4\pi\mu^0}\delta_{ij}\Phi_{,m} - \frac{1}{16\pi\mu^0(1-\nu^0)}\Psi_{,ijm})C_{jmkl}^0$	
Linear:	$g_{iklp}^{I1} = -(\frac{1}{4\pi\mu^0}\delta_{ij}\Phi_{p,m} - \frac{1}{16\pi\mu^0(1-\nu^0)}\Psi_{p,ijm})C_{jmkl}^0$	
Quadratic:	$g_{iklpq}^{I2} = -(\frac{1}{4\pi\mu^0}\delta_{ij}\Phi_{pq,m} - \frac{1}{16\pi\mu^0(1-\nu^0)}\Psi_{pq,ijm})C_{jmkl}^0$	

$$\Psi_{n,ijkl} = \frac{4\pi}{105}\begin{cases} -6(\delta_{in}\delta_{jk}r_l + \delta_{ik}\delta_{jn}r_l + \delta_{ij}\delta_{kn}r_l + \delta_{jk}\delta_{il}r_n + \delta_{jn}\delta_{il}r_k + \delta_{in}\delta_{jl}r_k + \delta_{ij}\delta_{nl}r_k \\ +\delta_{kn}\delta_{il}r_j + \delta_{ik}\delta_{nl}r_j + \delta_{jk}\delta_{nl}r_i + \delta_{jn}\delta_{kl}r_i + \delta_{in}\delta_{kl}r_j + \delta_{ij}\delta_{kl}r_n + \delta_{kn}\delta_{jl}r_i + \delta_{ik}\delta_{jl}r_n) & a \geq r \\ a^5\{(\frac{15a^2}{r^7} - \frac{21a^2}{r^5})(\delta_{in}\delta_{jk}r_l + \delta_{ik}\delta_{jn}r_l + \delta_{ij}\delta_{kn}r_l + \delta_{ik}\delta_{jl}r_n + \delta_{in}\delta_{jl}r_k + \delta_{ij}\delta_{nl}r_k \\ +\delta_{jn}\delta_{kl}r_i + \delta_{jk}\delta_{il}r_n + \delta_{kn}\delta_{il}r_j + \delta_{ik}\delta_{nl}r_j + \delta_{in}\delta_{kl}r_j + \delta_{ij}\delta_{kl}r_n + \delta_{jn}\delta_{il}r_k + \delta_{jk}\delta_{nl}r_i + \delta_{kn}\delta_{jl}r_i) \\ -105(\frac{a^2}{r^9} + \frac{1}{r^7})(\delta_{ik}r_jr_nr_l + \delta_{in}r_jr_kr_l + \delta_{ij}r_nr_kr_l + \delta_{jn}r_kr_ir_l \\ +\delta_{jk}r_ir_nr_l + \delta_{kn}r_ir_jr_l + \delta_{il}r_jr_kr_n + \delta_{jl}r_ir_kr_n + \delta_{kl}r_ir_jr_n + \delta_{nl}r_ir_jr_k) + 105(\frac{9a^2}{r^{11}} - \frac{7}{r^9})r_ir_jr_kr_nr_l\} & a < r \end{cases} \tag{A.20}$$

$$\Psi_{mn,ijkl} = \frac{4\pi}{315}\begin{cases} -10(\delta_{jn}\delta_{km}r_ir_l + \delta_{jm}\delta_{kn}r_ir_l + \delta_{in}\delta_{jk}r_mr_l + \delta_{ik}\delta_{jn}r_mr_l + \delta_{ij}\delta_{kn}r_mr_l \\ +\delta_{ij}\delta_{mn}r_nr_l + \delta_{im}\delta_{kn}r_jr_l + \delta_{in}\delta_{km}r_jr_l + \delta_{in}\delta_{jm}r_kr_l + \delta_{im}\delta_{jn}r_kr_l \\ +\delta_{jk}\delta_{il}r_mr_n + \delta_{km}\delta_{il}r_jr_n + \delta_{kn}\delta_{il}r_jr_m + \delta_{ik}\delta_{nl}r_jr_m \\ +\delta_{jn}\delta_{kl}r_mr_i + \delta_{in}\delta_{kl}r_mr_j + \delta_{ij}\delta_{kl}r_mr_n + \delta_{jm}\delta_{kl}r_ir_n + \delta_{im}\delta_{nl}r_jr_k \\ +\delta_{jk}\delta_{ml}r_ir_n + \delta_{km}\delta_{jl}r_ir_n + \delta_{kn}\delta_{jl}r_ir_m + \delta_{ik}\delta_{jl}r_nr_m \\ +\delta_{jn}\delta_{ml}r_kr_i + \delta_{in}\delta_{ml}r_kr_j + \delta_{ij}\delta_{ml}r_kr_n + \delta_{jm}\delta_{il}r_kr_n + \delta_{im}\delta_{jl}r_nr_k \\ +\delta_{jk}\delta_{nl}r_ir_m + \delta_{km}\delta_{nl}r_ir_j + \delta_{kn}\delta_{ml}r_ir_j + \delta_{ik}\delta_{ml}r_nr_j \\ +\delta_{jn}\delta_{il}r_kr_m + \delta_{in}\delta_{jl}r_kr_m + \delta_{ij}\delta_{nl}r_kr_m + \delta_{jm}\delta_{nl}r_kr_i + \delta_{im}\delta_{kl}r_nr_j) \\ +8a^4(\delta_{jk}\delta_{mn}r_ir_l + \delta_{ik}\delta_{mn}r_jr_l + \delta_{ij}\delta_{mn}r_kr_l + \delta_{mn}\delta_{il}r_jr_k + \delta_{mn}\delta_{jl}r_ir_k + \delta_{mn}\delta_{kl}r_ir_j) \\ -(12a^6 - 4a^4r^2)(\delta_{jk}\delta_{mn}\delta_{il} + \delta_{ik}\delta_{mn}\delta_{jl} + \delta_{ij}\delta_{mn}\delta_{kl}) & a \geq r \\ a^7[(\frac{-5a^2}{r^7} + \frac{9}{r^5})(\delta_{in}\delta_{jk}\delta_{ml} + \delta_{ik}\delta_{jn}\delta_{ml} + \delta_{ij}\delta_{kn}\delta_{ml} + \delta_{im}\delta_{jk}\delta_{nl} + \delta_{ik}\delta_{jm}\delta_{nl} + \delta_{ij}\delta_{km}\delta_{nl} \\ +\delta_{in}\delta_{km}\delta_{jl} + \delta_{im}\delta_{kn}\delta_{jl} + \delta_{in}\delta_{jm}\delta_{kl} + \delta_{im}\delta_{jn}\delta_{kl} + \delta_{jn}\delta_{km}\delta_{il} + \delta_{jm}\delta_{kn}\delta_{il}) \\ +(-\frac{5a^6}{r^7} + \frac{18a^4}{r^5} - \frac{21a^2}{r^3})(\delta_{ik}\delta_{mn}\delta_{jl} + \delta_{ij}\delta_{mn}\delta_{kl} + \delta_{jk}\delta_{mn}\delta_{il}) \\ +(\frac{35a^2}{r^9} - \frac{45}{r^7})(\delta_{in}\delta_{jk}r_mr_l + \delta_{ik}\delta_{jn}r_mr_l + \delta_{ij}\delta_{kn}r_mr_l + \delta_{im}\delta_{jk}r_nr_l + \delta_{ik}\delta_{jm}r_nr_l \\ +\delta_{ij}\delta_{km}r_nr_l + \delta_{in}\delta_{km}r_jr_l + \delta_{im}\delta_{kn}r_jr_l + \delta_{in}\delta_{jm}r_kr_l + \delta_{im}\delta_{jn}r_kr_l + \delta_{jn}\delta_{km}r_ir_l \\ +\delta_{jm}\delta_{kn}r_ir_l + \delta_{ml}\delta_{ik}r_nr_j + \delta_{nl}\delta_{ik}r_mr_j + \delta_{jl}\delta_{ik}r_mr_n + \delta_{jl}\delta_{im}r_nr_k + \delta_{nl}\delta_{im}r_jr_k \\ +\delta_{kl}\delta_{im}r_jr_n + \delta_{in}\delta_{jl}r_mr_k + \delta_{in}\delta_{ml}r_jr_k + \delta_{in}\delta_{kl}r_jr_m + \delta_{ij}\delta_{nl}r_mr_k + \delta_{ij}\delta_{ml}r_nr_k \\ +\delta_{ij}\delta_{kl}r_nr_m + \delta_{jm}\delta_{kl}r_nr_i + \delta_{jm}\delta_{nl}r_ir_k + \delta_{jm}\delta_{il}r_kr_n + \delta_{jn}\delta_{il}r_kr_m + \delta_{jn}\delta_{kl}r_mr_i \\ +\delta_{jn}\delta_{ml}r_ir_k + \delta_{jk}\delta_{il}r_nr_m + \delta_{jk}\delta_{nl}r_ir_m + \delta_{jk}\delta_{ml}r_ir_n + \delta_{kn}\delta_{il}r_jr_m + \delta_{kn}\delta_{jl}r_ir_m \\ +\delta_{ml}\delta_{kn}r_ir_j + \delta_{km}\delta_{il}r_jr_n + \delta_{jl}\delta_{km}r_ir_n + \delta_{nl}\delta_{km}r_ir_j) + (\frac{35a^6}{r^9} - \frac{90a^4}{r^7} + \frac{63a^2}{r^5})(\delta_{ik}\delta_{mn}r_jr_l \\ +\delta_{ij}\delta_{mn}r_kr_l + \delta_{jk}\delta_{mn}r_ir_l + \delta_{mn}\delta_{il}r_jr_k + \delta_{mn}\delta_{jl}r_ir_k + \delta_{kl}\delta_{mn}r_ir_j) \\ +5(\frac{-63a^2}{r^{11}} + \frac{63}{r^9})(\delta_{ik}r_lr_mr_nr_j + \delta_{im}r_lr_jr_nr_k + \delta_{in}r_lr_jr_mr_k + \delta_{ij}r_lr_nr_mr_k + \delta_{jm}r_lr_kr_nr_i \\ +\delta_{jn}r_lr_ir_kr_m + \delta_{jk}r_lr_ir_nr_m + \delta_{kn}r_lr_ir_jr_m + \delta_{km}r_lr_ir_jr_n + \delta_{ml}r_nr_ir_jr_k + \delta_{nl}r_mr_ir_jr_k \\ +\delta_{il}r_mr_nr_jr_k + \delta_{jl}r_mr_nr_ir_k + \delta_{kl}r_mr_nr_ir_j) \\ +(\frac{-385a^6}{r^{13}} + \frac{810a^4}{r^{11}} + \frac{-441a^2}{r^9})\delta_{mn}r_ir_jr_kr_l + 315(\frac{11a^2}{r^{13}} - \frac{9}{r^{11}})r_mr_nr_ir_jr_kr_l] & a < r \end{cases} \tag{A.21}$$

A.3. Eshelby's tensor in terms of the integrals of the potentials

For a distributed source field on a spherical inclusion, the material's response can be shown with Eshelby's tensors at the different orders in polynomial form, which can be written in terms of the integrals of the potentials (see Table A.2).

Classical Eshelby's tensor is defined by:

$S_{ijkl} = \frac{g_{ikl,j}+g_{jkl,i}}{2}$, $S_{ijklp} = \frac{g_{iklp,j}+g_{jklp,i}}{2}$, $S_{ijklpq} = \frac{g_{iklpq,j}+g_{jklpq,i}}{2}$,

Thermoelastic Eshelby's tensor as:

$R_{ijk} = \frac{w_{ik,j}+w_{jk,i}}{2}$, $R_{ijkp} = \frac{w_{ikp,j}+w_{jkp,i}}{2}$, $R_{ijkpq} = \frac{w_{ikpq,j}+w_{jkpq,i}}{2}$.

References

Alzebdeh, K., Jasiuk, I., Ostoja-Starzewski, M., 1998. Scale and boundary conditions effects in elasticity and damage mechanics of random composites. In: Damage Mechanics in Engineering Materials. Elsevier, pp. 65–80. http://dx.doi.org/10.1016/s0922-5382(98)80035-4.

Barber, J., 1992. Elasticity. Springer Dordrecht, Dordrecht, http://dx.doi.org/10.1007/978-94-011-2454-6.

Barmouz, M., Asadi, P., Givi, M.B., Taherishargh, M., 2011. Investigation of mechanical properties of Cu/SiC composite fabricated by FSP: Effect of SiC particles' size and volume fraction. Mater. Sci. Eng. A 528 (3), 1740–1749. http://dx.doi.org/10.1016/j.msea.2010.11.006.

Bažant, Z.P., 1999. Size effect on structural strength: a review. Arch. Appl. Mech. 69, 703–725. http://dx.doi.org/10.1007/s004190050252.

Biot, M.A., 1956. Thermoelasticity and irreversible thermodynamics. J. Appl. Phys. 27 (3), 240–253. http://dx.doi.org/10.1063/1.1722351.

Campanella, R.G., Mitchell, J.K., 1968. Influence of temperature variations on soil behavior. J. Rock Mech. Geotech. Eng. 94 (3), http://dx.doi.org/10.1061/JSFEAQ.0001136.

Dirrenberger, J., Forest, S., Jeulin, D., 2014. Towards gigantic RVE sizes for 3D stochastic fibrous networks. Int. J. Solids Struct. 51 (2), 359–376. http://dx.doi.org/10.1016/j.ijsolstr.2013.10.011.

Eshelby, J.D., 1957. The determination of the elastic field of an ellipsoidal inclusion, and related problems. Proc. R. Soc. A 241 (1226), 376–396. http://dx.doi.org/10.1098/rspa.1957.0133.

Eshelby, J.D., 1959. The elastic field outside an ellipsoidal inclusion. Proc. R. Soc. A 252 (1271), 561–569. http://dx.doi.org/10.1098/rspa.1959.0173.

Haynes, W.M., 2014. CRC Handbook of Chemistry and Physics. CRC Press, http://dx.doi.org/10.1201/b17118.

Hill, R., 1963. Elastic properties of reinforced solids: Some theoretical principles. J. Mech. Phys. Solids 11 (5), 357–372. http://dx.doi.org/10.1016/0022-5096(63)90036-x.

Hori, M., Nemat-Nasser, S., 1999. On two micromechanics theories for determining micro–macro relations in heterogeneous solids. Mech. Mater. 31 (10), 667–682. http://dx.doi.org/10.1016/S0167-6636(99)00020-4.

Kanit, T., Forest, S., Galliet, I., Mounoury, V., Jeulin, D., 2003. Determination of the size of the representative volume element for random composites: statistical and numerical approach. Int. J. Solids Struct. 40 (13–14), 3647–3679. http://dx.doi.org/10.1016/s0020-7683(03)00143-4.

Kováčik, J., Marsavina, L., Linul, E., 2018. Poisson's ratio of closed-cell aluminium foams. Materials 11 (10), 1904. http://dx.doi.org/10.3390/ma11101904.

Kushch, V.I., 1997. Microstresses and effective elastic moduli of a solid reinforced by periodically distributed spheroidal particles. Int. J. Solids Struct. 34 (11), 1353–1366. http://dx.doi.org/10.1016/S0020-7683(96)00078-9.

Kushch, V.I., 2020. Elastic fields and effective stiffness of ellipsoidal particle composite using the representative unit cell model and multipole expansion method. Internat. J. Engrg. Sci. 154, 103336. http://dx.doi.org/10.1016/j.ijengsci.2020.103336.

Lee, H., Choi, C.-w., Jin, J.-w., Huh, M., Lee, S., Kang, K.-w., 2019. Homogenization-based multiscale analysis for equivalent mechanical properties of nonwoven carbon-fiber fabric composites. J. Mech. Sci. Technol. 33, 4761–4770. http://dx.doi.org/10.1007/s12206-019-0917-6.

Li, Y., Bushby, A.J., Dunstan, D.J., 2016. The Hall–Petch effect as a manifestation of the general size effect. Proc. R. Soc. A 472 (2190), 20150890. http://dx.doi.org/10.1098/rspa.2015.0890.

Liu, Y.J., Song, G., Yin, H.M., 2015. Boundary effect on the elastic field of a semi-infinite solid containing inhomogeneities. Proc. R. Soc. A 471 (2179), 20150174. http://dx.doi.org/10.1098/rspa.2015.0174.

Mura, T., 1987. Micromechanics of Defects in Solids. Springer Netherlands, Dordrecht, http://dx.doi.org/10.1007/978-94-009-3489-4.

Nemat-Nasser, S., Hori, M., 2013. Micromechanics: Overall Properties of Heterogeneous Materials. Elsevier.

Nowacki, W., 1986. Thermoelasticity, Second edn. Pergamon Press, OXford, http://dx.doi.org/10.1016/C2013-0-03247-1.

Ostoja-Starzewski, M., 1998. Random field models and scaling laws of heterogenous media. Arch. Mech. 50 (3), 549–558.

Pan, H., Feng, Y.P., 2008. Semiconductor nanowires and nanotubes: Effects of size and surface-to-volume ratio. ACS Nano 2 (11), 2410–2414. http://dx.doi.org/10.1021/nn8004872.

Prasad, N.N.V., Aliabadi, M.H., Rooke, D.P., 1994. The dual boundary element method for thermoelastic crack problems. Int. J. Fract. 66 (3), 255–272. http://dx.doi.org/10.1007/bf00042588.

Song, G., Wang, L., Deng, L., Yin, H., 2015. Mechanical characterization and inclusion based boundary element modeling of lightweight concrete containing foam particles. Mech. Mater. 91, 208–225. http://dx.doi.org/10.1016/j.mechmat.2015.07.014.

Tavman, I., 1996. Thermal and mechanical properties of aluminum powder-filled high-density polyethylene composites. J. Appl. Polym. Sci. 62 (12), 2161–2167. http://dx.doi.org/10.1002/(SICI)1097-4628(19961219)62:12<2161::AID-APP19>3.0.CO;2-8.

Terada, K., Hori, M., Kyoya, T., Kikuchi, N., 2000. Simulation of the multi-scale convergence in computational homogenization approaches. Int. J. Solids Struct. 37 (16), 2285–2311. http://dx.doi.org/10.1016/s0020-7683(98)00341-2.

Verruijt, A., 1969. The completeness of Biot's solution of the coupled thermoelastic problem. Quart. Appl. Math. 26 (4), 485–490. http://dx.doi.org/10.1090/qam/239802.

Wang, T., Wu, C., Zhang, L., Yin, H., 2022. The green's function-based thermal analysis of a spherical geothermal tank in a semi-infinite domain. J. Appl. Mech. 89 (7), 071008. http://dx.doi.org/10.1115/1.4054568.

Wisnom, M.R., 1999. Size effects in the testing of fibre-composite materials. Compos. Sci. Technol. 59 (13), 1937–1957. http://dx.doi.org/10.1016/S0266-3538(99)00053-6.

Wu, C., Wang, T., Yin, H., 2023a. The Green's function based thermoelastic analysis of a spherical geothermal tank in a semi-infinite domain. J. Mech. Phys. Solids 173, 105207. http://dx.doi.org/10.1115/1.4054568.

Wu, C., Yin, H., 2021. The inclusion-based boundary element method (iBEM) for virtual experiments of elastic composites. Eng. Anal. Bound. Elem. 124, 245–258. http://dx.doi.org/10.1016/j.enganabound.2020.12.020.

Wu, C., Zhang, L., Cui, J., Yin, H., 2022. Three dimensional elastic analysis of a bi-material system with a single domain boundary element method. Eng. Anal. Bound. Elem. http://dx.doi.org/10.1016/j.enganabound.2022.09.037.

Wu, C., Zhang, L., Weng, G.J., Yin, H., 2024. Thermomechanical modeling of functionally graded materials based on bimaterial fundamental solutions. International Journal of Engineering Science 198, 104040. http://dx.doi.org/10.1016/j.ijengsci.2024.104040.

Wu, C., Zhang, L., Yin, H., 2023b. Effect of defects and reinforcements on the mechanical behaviour of a bi-layered panel. Proc. R. Soc. A 479 (2271), http://dx.doi.org/10.1098/rspa.2022.0754.

Xu, H.H., Ostertag, C.P., Braun, L.M., Lloyd, I.K., 1994. Effects of fiber volume fraction on mechanical properties of SiC-fiber/Si3N4-matrix composites. J. Am. Ceram. Soc. 77 (7), 1897–1900. http://dx.doi.org/10.1111/j.1151-2916.1994.tb07068.x.

Yin, H., Song, G., Zhang, L., Wu, C., 2022. The Inclusion-Based Boundary Element Method (iBEM). Academic Press, http://dx.doi.org/10.1016/C2018-0-04857-4.

Yin, H., Zadshir, M., Pao, F., 2021. Building Integrated Photovoltaic Thermal Systems: Fundamentals, Designs and Applications. Academic Press, http://dx.doi.org/10.1016/C2019-0-02586-1.

Yin, H., Zhao, Y., 2016. Introduction to the Micromechanics of Composite Materials. CRC Press, http://dx.doi.org/10.1201/b19685.

Zhang, H., Li, Y., Tang, Q., Liu, L., Zhou, Z., 2012. First-principles studies on structural and electronic properties of GaN–AlN heterostructure nanowires. Nanoscale 4 (4), 1078–1084. http://dx.doi.org/10.1039/C1NR10465A.

Zhang, L., Lin, Q., Chen, F., Zhang, Y., Yin, H., 2020. Micromechanical modeling and experimental characterization for the elastoplastic behavior of a functionally graded material. Int. J. Solids Struct. 206, 370–382. http://dx.doi.org/10.1016/j.ijsolstr.2020.09.010.